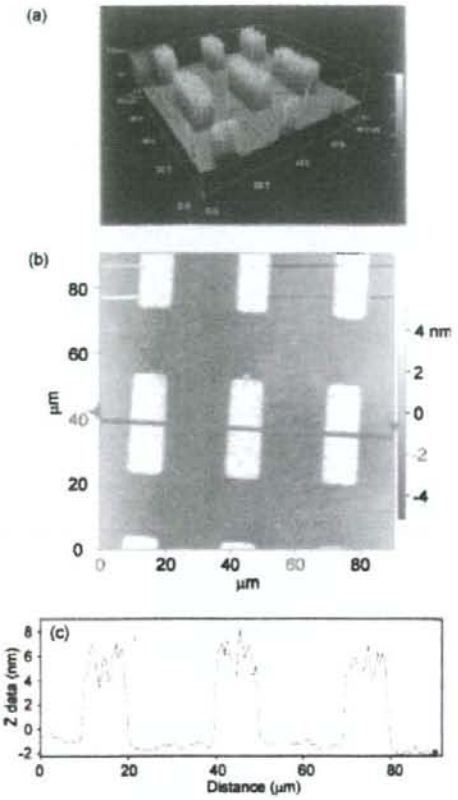

Figure 3. AFM images of rHSA-nanosheets adsorbed onto the patterned ODS-SAM. (a) 3-D image, (b) top view image, and (c) cross-sectional image. [Color figure can be viewed in the online issue, which is available at www.interscience.wiley.com.]

sheets. The rectangular patterns (10 μm × 30 μm) were vividly embossed by rHSA, and nonspecific adsorption of rHSA was scarcely observed on the SiO_2 regions. From the AFM cross-sectional image, the thickness of the rHSA-nanosheets plus the ODS-SAM was estimated to be 6.6 ± 1.0 nm as shown in Figure 3(b,c). On the other hand, the thickness of the ODS-SAM itself was estimated to be 2.1 ± 0.7 nm (data not shown). Based on the difference between both thicknesses, the thickness of the rHSA-nanosheets was calculated to be 4.5 ± 1.0 nm, which agrees with the dimensions of rHSA.

rHSA-nanosheets having heterosurfaces

For fabrication of the rHSA-nanosheets having heterosurfaces, we conjugated NBD-labeled latex beads to the obverse side of TRITC-labeled rHSA-nanosheets on ODS-SAM. After the rHSA-nanosheets were detached from the ODS-SAM by the surfactant treatment, the dispersion was put on the cover glass plate, and then the sheets were observed with a confocal laser scanning microscope. There were abundant rectangular rHSA-nanosheets in various conformations (10 μm × 30 μm). We focused on a sheet adopting a bent form as shown in Figure 4. When the rhodamine-labeled rHSA of the sheets was excited at 543 nm, the entire sheet turned red with a measured emission wavelength of over 570 nm as shown in Figure 4(a). On the other hand, NBD of the latex beads was excited at a wavelength of 458 nm and detected in the emission wavelength region from 500 to 530 nm. We observed that the majority of the surface of the sheets turned yellow, and the bent site of the nanosheet was quenched due to the fluorescent resonance energy transfer (FRET) effect from the NBD to the rhodamine as shown in Figure 4(b). When these pictures (a) and (b) were overlayed, the resulting picture (c) clearly showed the red and yellow heterosurfaces, suggesting that NBD-labeled latex beads adhered to the reverse surface at the bent site of the rHSA-nanosheet. Finally, we observed the latex beads-conjugated rHSA-nanosheets on ODS-SAM using an SEM. Many latex beads were specifically conjugated to the obverse side of the rHSA-nanosheets. The contrast of the rHSA-nanosheet was clear and uniform in comparison with that of SiO_2 region as shown in Figure 4(e,f), suggesting that the rHSA-nanosheets were thin and flat.

DISCUSSION

The purpose of this article is to propose a novel method to prepare free-standing biocompatible nanosheets having heterosurfaces, as a new biomaterial, by a combination of four processes as shown in Figure 1: (1) specific adsorption of rHSA molecules onto patterned hydrophobic ODS-SAM regions, (2) preparation of nanosheets of SH-rHSA via two-dimensionally disulfide crosslinking, (3) surface modification of the resulting nanosheets, and (4) preparation of free-standing nanosheets by detachment from the ODS-SAM.

We selected hydrophobic ODS having a terminal CH_3 group for the SAM. Wadu-Mestheige et al. reported that bovine serum albumin could be selectively adsorbed on the SAM regions having a terminal CH_3 in comparison with SAM regions having a terminal OH or COOH.[26] Since the resulting water contact angle of the ODS-SAM was similar to that of the ODS-SAM in the previous reports,[27,28] we could confirm that the hydrophobic ODS-SAM was certainly constructed on the silicon oxide (Table I).

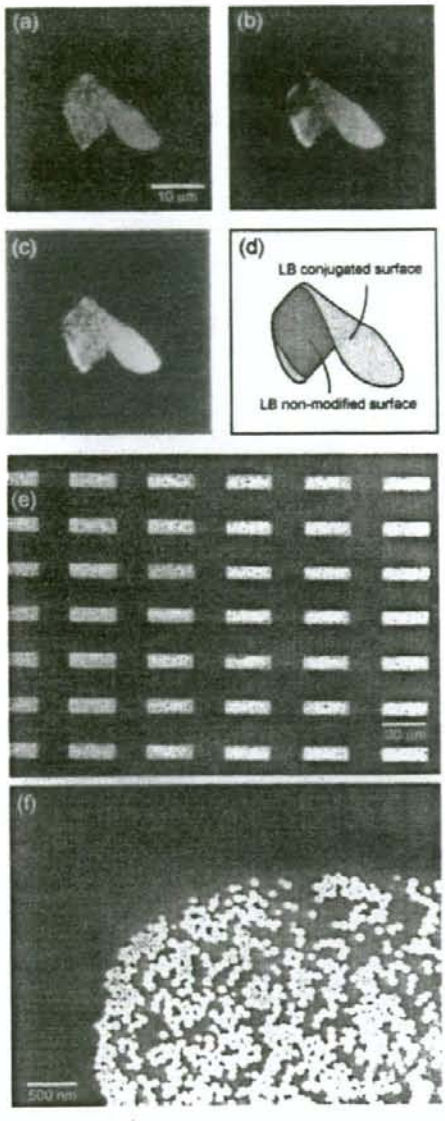

Figure 4. Confocal laser scanning microscopic images of rhodamine-labeled rHSA-nanosheets, of which the obverse sides were modified with NBD-labeled latex beads. (a) Rhodamine-conjugated rHSA was excited at a wavelength of 543 nm, and the emission wavelength detected at over 570 nm, (b) NBD conjugated latex beads were excited at a wavelength of 458 nm and the emission wavelength detected at 500–530 nm, (c) the overlayed image of (a) and (b), and (d) Schematic image of rhodamine-labeled rHSA-nanosheets, of which the obverse sides were modified with NBD-labeled latex beads. (e) SEM image of rHSA-nanosheets, of which the obverse sides were modified with latex beads. (f) Magnified SEM image of (e).

As a first step, we investigated the suitable conditions (pH and concentration) for rHSA adsorption onto the ODS-SAM. At pH 7.4, the rHSA molecules did not adsorb on the ODS-SAM, as seen from the contact angle measurement (Table I). At that pH, the charge of rHSA is negative, because the isoelectric point of rHSA is 4.9. Above that pH, rHSA molecules have little hydrophobic interaction with ODS-SAM and repel each other electrostatically. Therefore, they favor remaining dissociated in the solution rather than to assemble onto the ODS-SAM, resulting in no change in the contact angle. At pH 5.0, near the isoelectric point of rHSA, the contact angle was significantly decreased, suggesting that the rHSA molecules were firmly adsorbed on the ODS-SAM. As described later in the final step, the water contact angle after the surfactant treatment was comparable to that of the ODS-SAM before rHSA adsorption, indicating that the attractive force giving rise to the adsorption of rHSA on the ODS-SAM was hydrophobic interaction. These results are consistent with the previous reported experiments on albumin adsorption at pH 5.0 and influences the three-dimensional shape of the individual albumin adsorbed on the terminal CH_3 of SAM.[29,30] These previous studies reported on the adsorption mechanism of albumin onto the SAM as the following: the electrostatic repulsion among albumin molecules was decreased at pH 5.0 and the interprotein interaction (mostly hydrophobic interaction) strengthened, thus the albumin immobilized on the SAM was more stable than individual proteins in the solution state.

Next, at pH 5.0 and r.t., we explored the optimum concentration of the TRITC-labeled SH-rHSA adsorbed on the patterned ODS-SAM. In the case of the TRITC-labeled SH-rHSA at a concentration of 10 μg/mL or over, the rectangular patterns were distinctly stained by fluorescence; however, the SH-rHSA molecules were nonspecifically adsorbed on the hydrophilic silicon oxide regions and brightened the background (data not shown). In the case of the SH-rHSA at a concentration of 0.1 μg/mL, the ODS patterns were hardly stained (data not shown). At a concentration of 1 μg/mL, almost all the ODS patterns were selectively stained (Fig. 2) and the rHSA molecules were predominantly located in the patterned ODS region (Fig. 3). The number of the ODS patterns arranged on the substrate (1 cm × 1 cm) is estimated to be $\sim 6.7 \times 10^4$, and the number of rHSA molecules adsorbed on one patterned ODS region was calculated to be $\sim 1.2 \times 10^7$ molecules, if the average surface area of one rHSA molecule is 25.5 nm^2,[31] and rHSA molecules are closely packed in the patterned ODS region (rectangular patterns: 10 μm × 30 μm, area: 3.0×10^8 nm^2). Accordingly, the total number of the rHSA molecules adsorbing on the ODS patterns was calculated to be $\sim 8.0 \times 10^{11}$ mole-

cules. Approximately 9% of the total rHSA was estimated to be adsorbed onto the ODS regions by immersing the substrate in the 1 mL rHSA solution at a concentration of 1 μg/mL, containing 9.0×10^{12} rHSA molecules. This was also supported by the results obtained from the other patterns such as circles and squares (data not shown). Consequently, we set the conditions of the rHSA adsorption onto the patterned ODS-SAM, at pH 5.0, at r.t. and the concentration of 1 μg/mL.

The second step of the process is to crosslink each SH-rHSA molecule adsorbed on the patterned ODS-SAM to prepare nanosheets. We presumed that once the SH-rHSA molecules were adsorbed onto the substrate they would closely pack in the pattern, and thus be easy to crosslink in comparison with those in an aqueous solution. We utilized the crosslinking conditions for SH-rHSA in an aqueous solution to estimate the necessary conditions for crosslinking on the ODS-SAM. Crosslinking of the SH-rHSA by *N*-succinimidyl 3-(2-pyridyldithio) propionate (SPDP, spacer length is 0.68 nm), which has a terminal succinimidyl group and a pyridyldisulfide group to introduce the SH group to the surface of rHSA molecule after a DTT treatment, failed probably because the spacer length of SPDP would be too short to crosslink. Referring to a report by Komatsu et al., where a dimer and clusters of rHSA had been exquisitely synthesized using a bis-maleimidohexane and an LC-SPDP, which have spacer lengths of 1.61 and 1.57 nm, respectively,[31,32] we used the LC-SPDP, which has similar functionality as that of SPDP. Only a small proportion of the SH-rHSA molecules crosslink at pH 7.4 in the presence of copper ion (II) as described in a previous report,[25] suggesting that the rHSA molecules electrostatically repel each other because of the negative ζ-potential of the rHSA molecule. At pH 5.0, near the isoelectric point (p*I* = 4.9), the SH-rHSA was significantly crosslinked. The percentage of the peak areas of the void fractions for the total peak areas, which corresponded to the amount of the crosslinked rHSA over the molecular weight of 670 kDa, increased with the increasing number of the SH groups bound to one rHSA molecule. On the other hand, the crosslinking of the SH-rHSA was extremely slow in the absence of copper ion (II). The thiol oxidation is commonly facilitated in alkaline conditions because of complexation of copper ion (II) with thiolate anions.[25] However, we used the weakly acidic conditions (pH 5.0), where the reaction rate was considered to be slow, suggesting that the thiol oxidation of the rHSA molecules would be controlled by electrostatic repulsion and hydrophobic interaction of rHSA molecules. Based on the earlier results, we could crosslink the SH-rHSA molecules adsorbed on the patterned ODS-SAM at pH 5.0 in the presence of 1 μ*M* copper ion (II).

We measured the thickness of the rHSA-nanosheets as 4.5 ± 1.0 nm from the thickness of the ODS-SAM alone and the rHSA-nanosheet adsorbed on the ODS-SAM using AFM (Fig. 3). Carter and Ho reported that the tertiary structure of the HSA molecule determined from X-ray diffractometry could be described as a heart-shaped or equilateral triangular molecule, with each side 8 nm in length and with an average thickness of 3 nm.[33] The result showed that the rHSA-nanosheets could be regarded as a monolayer of SH-rHSA. As the hydrophobic interaction of SH-rHSA molecules with ODS-SAM should be stronger than that of SH-rHSA molecules with each other, the rHSA molecules weakly adsorbed onto the rHSA monolayer could be removed by washing before the addition of copper ion (II) as a catalyst of disulfide crosslinking. Furthermore, we confirmed that the nonspecific adsorption onto the SiO_2 surface was extremely reduced if the substrate were immersed into the rHSA solution under the aforementioned conditions, based on the results obtained by AFM as well as fluorescent microscopy.

In the third step, we tried to modify the surface of the resulting nanosheet with latex beads, which were useful carriers because of their uniform size and ease of confirmation by microscopic observation. We conjugated the NBD-labeled latex beads onto the obverse side of the TRITC-labeled rHSA-nanosheets that had been adsorbed on the ODS-SAM and demonstrated the preparation of nanosheets having heterosurfaces. As shown in Figure 4, there were many rHSA-nanosheets in various conformations of rectangles, such as bent forms. Surprisingly, there were no broken sheets, suggesting that the rHSA-nanosheets are tough and extremely flexible. Focusing on the nanosheet having a bent form (Fig. 4), when the rhodamine-labeled sheets were excited at 543 nm, the entire sheet turned red with a measured emission wavelength of over 570 nm [Fig. 4(a)]. On the other hand, we tried to detect the NBD on the surface of the sheet as yellow at the excitation of 458 nm and at the emission wavelength region from 500 to 530 nm. We could observe that the obverse surface of the sheet was colored yellow, and the reverse side (bent site) was significantly quenched [Fig. 4(b)]. Since the FRET efficiency is related to the inverse six power of the distance between the acceptor and donor probes, the technique is elegantly used to measure the molecular distance at the 1.5–7.5 nm range.[34,35] Based on the earlier information and judging from the thickness of the rHSA-nanosheet, the quenching of the NBD emission from the bent side of the nanosheet was caused by the FRET effect from NBD to rhodamine. It also indicates that the NBD-latex beads are attached only to the obverse side of the nanosheet. If a sufficient amount of the NBD-latex beads were attached to both sides of the

sheet, then both sides of the sheet would be quenched. Furthermore, we also confirmed that the latex beads were specifically conjugated to the obverse side of the rHSA-nanosheets using an SEM [Fig. 4(e,f)]. The nanosheets released from the substrate after conjugating the latex beads were heterogeneously modified.

In the final step, we investigated a method to detach the rHSA-nanosheets from the patterned ODS-SAM. We selected $C_{12}E_{10}$ as a nonionic surfactant for which surfactant ability was independent of pH change. As shown in Table I, when the substrate, to which rHSA (non-SH modification) molecules were adsorbed, was immersed into a 1% (v/v) solution of $C_{12}E_{10}$ for 1 h at r.t., the water contact angle was returned to that of the ODS-SAM before rHSA adsorption. This indicated that the rHSA adsorbed on the ODS-SAM was detached by the addition of a $C_{12}E_{10}$, and the attractive force giving rise to the adsorption of rHSA on the ODS-SAM was hydrophobic interaction. In the first and second processes, the SH-rHSA molecules were selectively adsorbed onto the patterned ODS regions and crosslinked in the presence of copper ion (II) to prepare the rHSA-nanosheets. Very few of the resulting nanosheets were detached from the substrate by immersion in the 1% $C_{12}E_{10}$ solution for 1 h, whereas the control rHSA could simply detach. It took at least 6 h to detach the nanosheet from the substrate with the 1% $C_{12}E_{10}$ solution. On the other hand, we also conformed that the nanosheets were completely dissolved after 1 h by a DTT treatment (data not shown). This suggested that it was difficult for the $C_{12}E_{10}$ molecules to diffuse into the spaces between the nanosheets and the ODS-SAM substrate, because the nanosheet was composed of sufficiently two-dimensionally crosslinked rHSA by intermolecular oxidation of thiol groups. Furthermore, we confirmed that the resulting rHSA-nanosheets were stable in the presence of $C_{12}E_{10}$, because the sheet shapes did not change after the $C_{12}E_{10}$ removal by dialysis (data not shown).

Using a confocal laser scanning microscopy, we fortunately observed the rHSA-nanosheets in three-dimensional images and confirmed them to be a curved form [Fig. 2(c), and figure of supporting information]. On the basis of analyses of quartz crystal microbalance and grazing angle infrared spectroscopy, Roach et al. reported that albumin had enough adsorption affinity toward the hydrophobic (CH_3 terminus) compared to the hydrophilic surface (OH terminus), to cause adsorption-induced deformation.[36] Furthermore, Zeng et al. showed through modeling that the orientation of the adsorbed protein (lysozyme) was dependent on the discrete organization of the functional groups presented on the SAM surface, and in the case of the hydrophobic CH_3 group, hydrophobic amino residues of the protein were closest to the surface.[37] From these references, we suggested that the rHSA-nanosheets would adopt a curved form, because the wettability of the obverse and reverse surface of the rHSA-nanosheets was different, that is, the obverse surface appeared to be more hydrophilic than the reverse surface. Consequently, we succeeded in the detachment of the rHSA-nanosheets from the ODS-SAM by mild conditions such as surfactant immersion in order to obtain uniform rHSA-nanosheets.

CONCLUSIONS

We succeeded in the preparation of free-standing rectangular (10 × 30 μm) and ultrathin (4.5 ± 1.0 nm) rHSA-nanosheets by two-dimensional crosslinking via disulfide bonds on a patterned ODS-SAM, and could also obtain free-standing rHSA-nanosheets having heterosurfaces by surface modification with fluorescent latex beads. Thus, the rHSA-nanosheets may be a suitable candidate as a new biomaterial for drug-delivery carriers, hemostatic reagents, wound dressing for burn injury, and so forth. In our future work, we are preparing the rHSA-nanosheets on a large scale to carry the recombinant fragments of platelet membrane protein and/or dodecapeptides such as GPIbα and H12 to evaluate their performance *in vitro* and *in vivo*.

Y.O. was the recipient of a Research Fellowships from the JSPS for Young Scientists and the recipient of Japan Health Sciences Foundation.

References

1. Tomii Y. Lipid formation as a drug carrier for drug delivery. Cur Pharma Design 2002;8:467–474.
2. Takeoka S, Teramura Y, Okamura Y, Handa M, Ikeda Y, Tsuchida E. Fibrinogen-conjugated albumin polymers and their interaction with platelets under flow conditions. Biomacromolecules 2001;2:1192–1197.
3. Takeoka S, Teramura Y, Ohkawa H, Ikeda Y, Tsuchida E. Conjugation of von Willebrand factor-binding domain of platelet glycoprotein Ibα to size-controlled albumin microspheres. Biomacromolecules 2000;1:290–295.
4. Teramura Y, Okamura Y, Takeoka S, Tsuchiyama H, Narumi H, Kainoh M, Handa M, Ikeda Y, Tsuchida E. Hemostatic effects of polymerized albumin particles bearing rGPIa/IIa in thrombocytopenic mice. Biochem Biophys Res Commun 2003; 306:256–260.
5. Okamura Y, Takeoka S, Teramura Y, Maruyama Y, Tsuchida E, Handa M, Ikeda Y. Hemostatic effects of fibrinogen-γ chain dodecapeptide-conjugated polymerized albumin particles *in vitro* and *in vivo*. Transfusion 2005;45:1221–1228.
6. Takeoka S, Teramura Y, Okamura Y, Tsuchida E, Handa M, Ikeda Y. Rolling properties of rGPIbα-conjugated phospholipid vesicles with different membrane flexibilities on vWf surface under flow conditions. Biochem Biophys Res Commun 2002;296:765–770.

7. Okamura Y, Maekawa I, Teramura Y, Maruyama Y, Tsuchida E, Handa M, Ikeda Y, Takeoka S. Hemostatic effects of phospholipid vesicles carrying fibrinogen-γ chain dodecapeptide *in vitro* and *in vivo*. Bioconjug Chem 2005;16:1589–1596.
8. Okamura Y, Handa M, Suzuki H, Ikeda Y, Takeoka S. New strategy of platelet substitutes for enhancing platelet aggregation at high shear rates; cooperative effects of a mixed system of fibrinogen γ-chain dodecapeptide- or glycoprotein Ibα-conjugated latex beads under flow conditions. J Artif Organs 2006;9:251–258.
9. Takeoka S, Okamura Y, Teramura Y, Watanabe N, Suzuki H, Tsuchida E, Handa M, Ikeda Y. Function of fibrinogen γ-chain dodecapeptide-conjugated latex beads under flow. Biochem Biophys Res Commun 2003;312:773–779.
10. Mattson J, Forrest JA, Borjesson L. Quantifying glass transition behaviour in ultrathin free-standing polymer films. Phys Rev E 2000;62:5187–5200.
11. Tang Z, Kotov NA, Magonov S, Ozturk B. Nanostructured artificial nacre. Nat Mater 2003;2:413–418.
12. Mallwitz F, Laschewsky A. Direct access to stable, freestanding polymer membranes by layer-by-layer assembly of polyelectrolytes. Adv Mater 2005;17:1296–1299.
13. Mamedov A, Kotov NA, Prato M, Guldi DM, Wicksted JP, Hirsch A. Molecular design of strong single-wall carbon nanotube/polyelectrolyte multiplayer composites. Nature Mater 2002;1:190–194.
14. Huck WT, Stroock AD, Whitesides GM. Synthesis of geometrically well-defined, molecularly thin polymer films. Angew Chem Int Ed 2000;39:1058–1061.
15. Mamedov A, Kotov N. Free-standing layer-by-layer assembled films of magnetite nanoparticles. Langmuir 2000;16:5530–5533.
16. Mallwitz F, Goedel WA. Physically cross-linked ultrathin elastomeric membranes. Angew Chem Int Ed 2001;40:2645–2647.
17. Eck W, Küller A, Grunze M, Völkel B, Gölzhäuser A. Freestanding nanosheets from crosslinked biphenyl self-assembled monolayers. Adv Mater 2005;17:2583–2587.
18. Xu H, Goedel WA. Polymer-silica hybrid monolayers as precursors for ultrathin free-standing porous membranes. Langumuir 2002;18:2363–2367.
19. Nardin C, Winterhalter M, Meier W. Giant free-standing ABA triblock copolymer membranes. Langmuir 2000;16:7708–7712.
20. Ulman A. An Introduction to Ultrathin Organic Films from Langmuir–Blodgett to Self-Assembly. San Diego, CA: Academic Press; 1991.
21. Khoshtariya DE, Wei J, Liu H, Yue H, Waldeck DH. Charge-transfer mechanism for cytochrome c adsorbed on nanometer thick films. Distinguishing frictional control from conformational gating. J Am Chem Soc 2003;125:7704–7714.
22. Ferapontova EE, Shipovskov S, Gorton L. Bioelectrocatalytic detection of theophylline at theophylline oxidase electrodes. Biosens Bioelectron 2007;22:2508–2515.
23. Niwa D, Yamada Y, Homma T, Osaka T. Formation of molecular templates for fabricating on-chip biosensing devices. J Phys Chem B 2004;108:3240–3245.
24. Sugimura H, Ushiyama H, Hozumi A, Takai O. Micropatterning of alkyl- and fluoroalkylsilane self-assembled monolayers using vacuum ultraviolet light. Langmuir 2000;16:885–888.
25. Cavallini D, De Marco C, Dupre S, Rotilio G. The copper-catalyzed oxidation of cysteine to cystine. Arch Biochem Biophys 1969;130:354–361.
26. Wadu-Mestherige K, Amro NA, Liu GU. Immobilization of proteins on self-assembled monolayers. Scanning 2000;22:380–288.
27. Siqueira PDF, Wenz G, Schunk P, Schimmel T. An improved method for the assembly of amino-terminated monolayers on SiO_2 and the vapor deposition of gold layers. Langmuir 1999;15:4520–4523.
28. Depalma V, Tillman N. Friction and wear of self-assembled trichlorosilane monolayer films on silicon. Langmuir 1989;5:868–872.
29. Norde W, Giesbers M, Pingsheng H. Langmuir–Blodgett films of polymerized 10,12-pentacosadiyonic acid as substrates for protein adsorption. Colloids Surf B 1995;5:255–263.
30. Prime KL, Whitesides GM. Adsorption of proteins onto surfaces containing end-attached oligo(ethylene oxide): A model system using self-assembled monolayers. J Am Chem Soc 1993;115:10714–10721.
31. Komatsu T, Oguro Y, Teramura Y, Takeoka S, Okai J, Anraku M, Otagiri M, Tsuchida E. Physicochemical characterization of cross-linked human serum albumin dimer and its synthetic heme hybrid as an oxygen carrier. Biochim Biophys Acta 2004;1675:21–31.
32. Komatsu T, Oguro Y, Nakagawa A, Tsuchida E. Albumin clusters: Structurally defined protein tetramer and oxygen carrier including thirty-two iron(II) porphyrins. Biomacromolecules 2005;6:3397–3403.
33. Carter DC, Ho JX. Structure of serum albumin. Adv Protein Chem 1994;45:153–204.
34. Stryer L, Haugland RP. Energy transfer: A spectroscopic ruler. Proc Natl Acad Sci USA 1967;58:719–726.
35. Stryer L. Fluorescence energy transfer as a spectroscopic ruler. Ann Rev Biochem 1978;47:819–946.
36. Roach P, Farrar D, Perry CC. Interpretation of protein adsorption: Surface-induced conformational changes. J Am Chem Soc 2005;127:8168–8173.
37. Zeng J, Li L, Chen S, Jiang S. Molecular simulation study of water interactions with oligo (ethylene glycol)-terminated alkanethiol self-assembled monolayers. Langmuir 2004;20:8931–8938.

Key Interactions in Integrin Ectodomain Responsible for Global Conformational Change Detected by Elastic Network Normal-Mode Analysis

Atsushi Matsumoto,*†‡ Tetsuji Kamata,§ Junichi Takagi,¶ Kenji Iwasaki,‡¶ and Kei Yura*†‡

*Quantum Bioinformatics Team, Center for Computational Science and Engineering, and †Research Unit for Quantum Beam Life Science Initiative, Quantum Beam Science Directorate, Japan Atomic Energy Agency, Kizugawa, Kyoto 619-0215, Japan; ‡CREST, Japan Science and Technology Agency, Kizugawa, Kyoto 619-0215, Japan; §Department of Anatomy, Keio University School of Medicine, Shinjuku, Tokyo 160-8582, Japan; and ¶Institute for Protein Research, Laboratory of Protein Synthesis and Expression, Osaka University, Suita, Osaka 565-0871, Japan

ABSTRACT Integrin, a membrane protein with a huge extracellular domain, participates in cell-cell and cell-extracellular-matrix interactions for metazoan. A group of integrins is known to perform a large-scale structural change when the protein is activated, but the activation mechanism and generality of the conformational change remain to be elucidated. We performed normal-mode analysis of the elastic network model on integrin $\alpha_V\beta_3$ ectodomain in the bent form and identified key residues that influenced molecular motions. Iterative normal-mode calculations demonstrated that the specific nonbonded interactions involving the key residues work as a snap to keep integrin in the bent form. The importance of the key residues for the conformational change was further verified by mutation experiments, in which integrin $\alpha_{IIb}\beta_3$ was used. The conservation pattern of amino acid residues among the integrin family showed that the characteristic pattern of residues seen around these key residues is found in the limited groups of integrin β-chains. This conservation pattern suggests that the molecular mechanism of the conformational change relying on the interactions found in integrin $\alpha_V\beta_3$ is unique to the limited types of integrins.

INTRODUCTION

Integrins are one of the metazoan protein families of adhesion receptors that mediate cell-cell and cell-extracellular-matrix interactions (1). In addition to this function, integrins transmit signals bidirectionally across the plasma membrane. Through these functions, integrins play key roles in diverse biological processes including cell migration, development, immune responses, and vascular hemostasis. They are therefore the target of effective therapeutic drugs against thrombosis and inflammation (1).

Integrin is a heterodimer transmembrane protein complex made of α- and β-chains. In mammals, 18 homologous α-chains and eight homologous β-chains are known so far, and different combinations of α- and β-chains have been identified. Integrins are not constitutively active as receptors. On cell surfaces, integrins are usually in a state of low affinity to their ligands (inactive state). By signals from inside the cell, integrins are supposed to be activated and function as receptors (inside-out signaling) (2).

Solution of the crystal structure of the ectodomain of integrin, $\alpha_V\beta_3$, was a major advance in the study of integrin (3). The crystal structure revealed that the head region was extremely bent over the two nearly parallel tails. Electron microscopy had shown that the integrin had an extended form (4–6), but later, the bent conformation of integrin was also observed. It was then shown that the bent conformation corresponded to the inactive state and the extended conformation to the active state, where integrin has high affinity to its ligand (7). The relationship between two conformations and two functional states is now well demonstrated. However, the transition mechanism between the two conformations is not yet understood.

Here, we studied the conformational changes of integrin ectodomain using normal-mode analysis (NMA) of the elastic network model of the protein. The application of conventional NMA to biomolecules, which employs realistic energy function in contrast to the NMA of the elastic network model, started more than 20 years ago (8–10). Since then, many biomolecules have been studied using NMA. This approach is widely used and has proved very effective for elucidating conformational fluctuations and changes related to biological functions. NMA of the elastic network model of a protein, which is directly related to this work, was first developed by Tirion (11), and the calculated normal modes were shown to faithfully reproduce the B-factors obtained from x-ray crystal structure analysis (12). It requires much fewer computational resources compared to the conventional

Submitted February 5, 2008, and accepted for publication May 6, 2008.

Address reprint requests to Atsushi Matsumoto, Quantum Bioinformatics Team, Center for Computational Science and Engineering, Japan Atomic Energy Agency, 8-1 Umemidai, Kizugawa, Kyoto 619-0215, Japan. Tel.: 81-774-71-3463; Fax: 81-774-71-3460; E-mail: matsumoto.atsushi@jaea.go.jp.

Kei Yura's present address is The Graduate School of Humanities and Sciences, Ochanomizu Univeristy, 2-1-1 Otsuka, Bunkyo, Tokyo 112-8610, Japan.

Editor: Peter Tieleman.

0006-3495/08/09/2895/14 $2.00

doi: 10.1529/biophysj.108.131045

method, so that the applications to huge macromolecular structures such as ribosomes and virus capsids (13–17) are possible. Here we applied the NMA of the elastic network model to the ectodomain of integrin $\alpha_V\beta_3$ in the bent form (inactive state). The analysis enabled us to identify the key residues that work as a switch for conformational changes of the integrin ectodomain. Iterative normal-mode calculations demonstrated that the key residues work as a snap to keep the structure in the bent form. The importance of the residues was further verified experimentally.

MATERIALS AND METHODS

Naming scheme for extracellular domains of integrin $\alpha_V\beta_3$

In this article, we follow the widely used naming scheme for the ectodomain of integrin $\alpha_V\beta_3$ (see Xiong et al. (3), for example). The α-chain consists of β-propeller (residues 1–438), thigh (439–592), calf-1 (602–738), and calf-2 (739–956) domains. The β-chain consists of PSI (1–54), hybrid (55–108 and 353–432), βA (109–352), EGF-1 and -2 (453–529), EGF-3 (532–562), EGF-4 (563–605), and βTD (606–690) domains. The PSI and EGF-1 and -2 domains are missing in the x-ray crystal structure to which we applied NMAs.

Elastic network model

In the usual treatment of an elastic network model (12,18), each residue in a protein is represented by the C_α atom. If the distance between two C_α atoms is less than the arbitrary chosen cutoff length, R_c (8–12 Å), the two residues are considered to be neighbors and the two C_α atoms are connected by a spring whose equilibrium length is the same as the distance in the initial conformation. Thus, the distance between the two C_α atoms is considered to be the distance between the two residues. The same spring constant C is used for all springs in the network model.

In this study, we defined the distance between two residues in a different way for the reason explained in the Results and Discussion section. We first considered all atoms except for hydrogens, and calculated the distances between all pairs of atoms. The shortest distance between atoms in two different residues was defined as the distance between the two residues, and if it was less than the arbitrary chosen cutoff length, r_c (3–5 Å), the two residues were considered to be neighbors. Once the neighbors were identified, each residue was represented by the C_α atom, and the C_α atoms in the neighbor residues were connected by springs with an arbitrarily chosen spring constant, C. The adjacent C_α atoms along the amino acid chain were automatically connected by this approach. We further introduced springs along the amino acid chain between C_α atoms in nth and $(n + 2)$th residues and between those in nth and $(n + 3)$th residues. The former spring restrained the fluctuations of the virtual bond angle formed by C_α atoms in nth, $(n + 1)$th and $(n + 2)$th residues, and the latter spring those of the virtual dihedral angle formed by C_α atoms in nth, $(n + 1)$th, $(n + 2)$th and $(n + 3)$th residues.

Normal-mode analysis of the elastic network model

The basic formulation of the NMA of the elastic network model is the same as that for the NMA performed with different coordinate systems and force fields (19–27):

The conformational potential energy of the system is approximated by the multidimensional parabola,

$$V = \frac{1}{2}\sum_{ij} f_{ij}\Delta q_i \Delta q_j, \tag{1}$$

where Δq_i is the instantaneous fluctuation of the ith generalized coordinate q_i from its equilibrium value and f_{ij} is an element of a Hessian matrix, F. The approximation is valid in the vicinity of minimum energy points.

The kinetic energy K is similarly expressed in quadratic form in terms of $\dot{q}_i$, the first derivative of q_i with respect to time, and coefficient h_{ij}, which is an element of the "mass" matrix, **H**:

$$K = \frac{1}{2}\sum_{ij} h_{ij}\Delta\dot{q}_i \Delta\dot{q}_j, \tag{2}$$

If the Δq_i and $\Delta\dot{q}_i$ are collected in the vectors $\Delta\mathbf{q}$ and $\Delta\dot{\mathbf{q}}$, respectively, Lagrange's equation of motion is simplified to

$$\mathbf{H}\Delta\ddot{\mathbf{q}} + \mathbf{F}\Delta\mathbf{q} = \mathbf{0}, \tag{3}$$

with a solution of the form

$$\Delta q_i = \sum_{n=1}^{N} A_{in}\alpha_n \cos(\omega_n t + \delta_n), \tag{4}$$

where N is the number of freedom in the system. The constant α_n and phase angle δ_n are determined from the initial conditions. The coefficient A_{in} is an element of a matrix **A** which simultaneously diagonalizes **H** and **F**; that is, $\mathbf{A}^T\mathbf{H}\mathbf{A} = \mathbf{I}$ and $\mathbf{A}^T\mathbf{F}\mathbf{A} = \mathbf{\Lambda}$, where $\mathbf{A}^T$ denotes the transposition of **A**, **I** is an identity matrix, and Λ is a diagonal matrix with elements $\Lambda_{nn} = \omega_n^2$.

In this study, the conformational potential energy of the elastic network model is expressed in the following form, as was done by Tirion (11):

$$V = \frac{1}{2}\sum_{(a,b)} C(|\mathbf{r}_{ab}| - |\mathbf{r}_{ab}^0|)^2, \tag{5}$$

where C is the spring constant, $\mathbf{r}_{ab}(= \mathbf{r}_b - \mathbf{r}_a)$ is the vector pointing from atom a to atom b, and the superscript zero indicates the initial conformation. Thus, the initial conformation has the minimum energy so that the energy minimization process is not necessary. In our treatment, each residue is represented by a C_α atom, and $\mathbf{r}_a$ and $\mathbf{r}_b$ are regarded as the positions of residues a and b, respectively. The summation is taken over all pairs of the neighboring residues.

If Eq. 5 is expanded about $\Delta\mathbf{r}_{ab}(= \mathbf{r}_{ab} - \mathbf{r}_{ab}^0)$ and terms higher than second order are ignored, it is simplified to

$$V = \frac{1}{2}\sum_{(a,b)} C\left(\frac{\mathbf{r}_{ab}^0 \cdot \Delta\mathbf{r}_{ab}}{|\mathbf{r}_{ab}^0|}\right)^2, \tag{6}$$

from which the Hessian matrix, F, is easily derived. We report the normalized normal-mode frequencies in the Results and Discussion section, because the normal-mode frequencies, which are obtained by diagonalizing the matrix F, are proportional to the square root of the arbitrarily chosen spring constant, C. Our system is described by the Cartesian coordinate, and thus the mass matrix **H** is a diagonal matrix with the $(3n - 2)$th, $(3n - 1)$th, and $3n$th diagonal elements equal to the total mass of the nth residue.

Comparison of thermal atomic fluctuations

To see how well the calculated values agreed with experimental values, the correlation coefficient was calculated using the equation

$$cc = \frac{\sum_{i=1}^{n}(x_i - \bar{x})(y_i - \bar{y})}{\sqrt{\sum_{i=1}^{n}(x_i - \bar{x})^2}\sqrt{\sum_{i=1}^{n}(y_i - \bar{y})^2}}, \tag{7}$$

where $\bar{x}$ is the average of x_i. In this study, the correlation coefficient between the thermal atomic fluctuations derived from the NMA and those derived

from the B-factors of the crystal structure was calculated. In the NMA, the thermal atomic fluctuations are given as a sum of contributions from all normal modes except for the six zero-frequency normal modes corresponding to the rigid body motions as a whole. The thermal atomic fluctuations of the crystal structure are proportional to the square root of the B-factors.

Similarity of two normal modes

We studied the effect of interactions between neighboring residues on the molecular motions to detect the key residues for the conformational changes of integrin. For this purpose, we compared low-frequency normal modes calculated for a model with full interactions to those for a model without specific interactions. The comparison of the two normal modes was made in terms of similarity, defined as

$$C_s = \left| \sum_k \mathbf{u}_k^i \cdot \mathbf{v}_k^j \right|, \tag{8}$$

where $\mathbf{u}_k^i$ and $\mathbf{v}_k^j$ are displacement vectors of the k th atom in the i th and j th normal modes, respectively, for the two elastic network models. Here, displacement vectors were normalized as

$$\sum_k \mathbf{u}_k^i \cdot \mathbf{u}_k^i = \sum_k \mathbf{v}_k^j \cdot \mathbf{v}_k^j = 1. \tag{9}$$

If the value is close to 1, the two normal modes are similar to each other. If it is close to zero, they are dissimilar.

Iterative normal-mode calculations

For the conventional NMA, a time-consuming energy minimization process is necessary before the NMA. For the NMA of the elastic network model, the energy minimization process is not necessary, and the NMA can be applied to any given conformation (28). If atoms in a protein are moved by a small amount from the initial positions along the displacement vectors in a normal mode, a slightly different new structure is generated. If the NMA of the elastic network model is applied to this new structure, another new structure can be obtained. By repeating this process, a series of structures is generated. This approach is often used for building atomic models based on electron microscopy density maps (29–31). Here, we call this series of calculations "iterative normal-mode calculation" and use this approach for forcing the conformational change of integrin from the bent to the extended forms and studying the role of the specific interactions in the conformational change.

The x-ray crystal structure of integrin (Protein Data Bank ID 1jv2 (3)) was used as the initial structure (the 0 th structure). After the nth NMA for the $(n-1)$th structure, many structures were generated by deforming the $(n-1)$th structure along each of the three lowest-frequency normal modes, and the structure with the largest distance between the head region and C-terminal end was chosen as the nth structure. The distance was measured between two C_α atoms in the residues Lys^{82} and Glu^{765} of the α-chain. The deformation was restricted so that the root mean-square displacement (rmsd) of the n th structure from the $(n-1)$th is <0.1 Å. The iterative calculation was terminated when the increment of distance between the head and C-terminal end of a new conformation (nth conformation) and that of the previous conformation was <0.1 Å.

Each time a new structure made of C_α atoms was generated by the approach described above, the coordinates of other atoms, which were necessary for updating the network formation, were determined by rigid-body treatment and a least-square fitting procedure (32) as follows. A structure made of a C_α atom in each residue (kth residue) and a few C_α atoms in the nearby residues along the amino acid chain in the x-ray crystal structure was treated as a rigid body and was fitted into the corresponding structure in the newly generated structure by rotational and translational manipulation in the least-square fitting procedure. The same manipulation was then applied to the other atoms in the kth residue of the x-ray crystal structure to get the positions of these atoms in the new structure. This process was repeated for all residues and the coordinates of all atoms in the new structure were obtained.

The purpose of the iterative normal-mode calculation in this study was to clarify the role of specific interactions in the conformational change from the bent to the extended form, in other words, to check whether the specific interactions obstructed the conformational change or not. For this purpose, two different iterative calculations were necessary. In one calculation, the specific interactions were kept, and in the other, they were not. However, the connectivity for the specific interactions could have changed during the iterative normal-mode calculation, because the network formation was to be updated each time a new structure was generated. To avoid this, we did not update the connectivity for the specific interactions during the iteration.

Multiple sequence alignment and conservation pattern of the residues

Homologous amino acid sequences to integrin from *Homo sapiens* $\alpha_V\beta_3$ were searched for out of all the amino acid sequences in UniProt (33) and all the translated amino acid sequences in DDBJ (34) by BLAST (35) with default parameters. Sequences derived from pseudogenes and partial sequences were eliminated. Identical sequences in the obtained set of sequences were grouped and only one of the sequences in each group was kept for building multiple sequence alignment. The multiple sequence alignment was built based on the progressive alignment method (36) using the BLOSUM62 matrix (37). Alignment at regions with extremely low sequence identity was manually adjusted based on the heuristic knowledge that cysteine residues should be well conserved and aligned among homologous extracellular domains. Sequences were grouped into clusters based on a phylogenetic tree built by the neighbor-joining method (38), with evolutionary distances calculated by the method of Kimura (39). The threshold for grouping the integrin sequences was set to be consistent with the annotation of sequences based on a previous study (1). Conservation of amino acid residues at positions of concern in each group was manually identified.

Mutation experiment to verify the activation mechanism

We experimentally verified the activation mechanism of integrin predicted by the NMA. We used integrin $\alpha_{IIb}\beta_3$ instead of $\alpha_V\beta_3$ for mutation experiments. Although the former is exclusively expressed on platelets and megakaryocytes different from the latter, and is known to use a different mechanism of signaling at the cytoplasmic domain of the α-chain (40), it has a common β_3-chain and binds to common ligands such as fibrinogen, fibronectin, and vitronectin in an RGD-dependent fashion. In addition to these structural and functional similarities, it has been well established that $\alpha_{IIb}\beta_3$ increases its affinity for fibrinogen by undergoing structural rearrangement upon inside-out signaling (41). Thus, we took advantage of the $\alpha_{IIb}\beta_3$-fibrinogen interactions to examine the effect of the mutations.

Normal mouse IgG was purchased from Sigma-Aldrich (St. Louis, MO). Anti-α_{IIb} monoclonal antibody (mAb) PL98DF6 (42) was a generous gift from Drs. J. Ylänne (University of Oulu, Oulu, Finland) and I. Virtanen (University of Helsinki, Helsinki, Finland). Anti-$\alpha_{IIb}\beta_3$-complex-specific activating mAb PT25-2 has previously been characterized (43). RPE-conjugated goat antimouse polyclonal antibody was purchased from Biosource (Camarillo, CA). The synthetic peptide Gly-Arg-Gly-Asp-Ser (GRGDS) was purchased from Peptide Research Institute (Osaka, Japan). Fluorescein-isothiocyanate (FITC) was purchased from Sigma-Aldrich. Human fibrinogen (Fbg) was purchased from Experimental Cell Research (South Bend, IN).

The full-length cDNAs for integrin α_{IIb} and β_3 subunits, generous gifts from Dr. Joseph C. Loftus (Mayo Clinic, Scottsdale, AZ), were cloned into the mammalian expression vector pBJ-1, kindly provided by Dr. Mark Davis (University of California, San Francisco, CA). The cDNAs for β_3 mutant L375A, L389A, R404A, R633A, R633del, R404A/R633A, R404A/R633del, and R404A/S674A were created by site-directed mutagenesis us-

ing the Transformer Site-Directed Mutagenesis Kit (BD Biosciences, San Jose, CA).

Chinese hamster ovary (CHO-K1) cells were cultured in Dulbecco's modified Eagle's medium (Invitrogen, Carlsbad, CA) supplemented with 10% fetal calf serum (Hyclone, Logan, UT), 1% penicillin and streptomycin (Invitrogen), and 1% nonessential amino acids (Sigma-Aldrich), and maintained at 37°C in a humidified incubator supplemented with 5% CO_2. Fifty micrograms of α_{IIb} cDNA construct was cotransfected with 50 μg of β_3 cDNA construct into CHO-K1 cells by electroporation. After 48 h, cells were detached and used for assays.

FITC-labeling of human Fbg is described in detail elsewhere (44). In brief, after adjusting the pH of human Fbg at 1 mg/ml in phosphate-buffered saline to 8.5 with 5% Na_2CO_3, 1/100 volume of 10 mg/ml FITC in dimethylsulfoxide was added and incubated at room temperature for 10 min. FITC-labeled Fbg was separated from free FITC on a PD-10 column (Amersham Biosciences, Uppsala, Sweden) equilibrated with HEPES-buffered saline (10 mM Hepes, 150 mM NaCl, pH 7.4). The concentration and *F/P* ratio of FITC-labeled Fbg were calculated as previously described (44). Forty-eight hours after transfection, cells were detached with phosphate-buffered saline containing 3.5 mM EDTA and incubated with nonfunctional anti-α_{IIb} mAb PL98DF6 followed by an RPE-conjugated F(ab')2 fragment of goat anti-mouse IgG. After washing, cells were incubated with FITC-labeled Fbg at 350 μg/ml with or without 1 mM GRGDS peptide in modified HEPES-Tyrode buffer (5 mM Hepes, 5 mM glucose, 0.2 mg/ml bovine serum albumin, and 1× Tyrode's solution) containing 1 mM $CaCl_2$ and 1 mM $MgCl_2$ for 2 h at 4°C. In some experiments, mAb PT25-2 was included at 10 μg/ml to activate $\alpha_{IIb}\beta_3$. After washing, fluorescence was measured on FACS Calibur. The median Fbg binding (FL1) to cell populations expressing high α_{IIb} (FL2 > 500) was calculated. Background binding in the presence of 1 mM GRGDS peptide was subtracted to obtain specific binding. Normalized Fbg binding was calculated by dividing the specific binding by the mean $\alpha_{IIb}\beta_3$ expression (FL2) of the gated population.

RESULTS AND DISCUSSION

Elastic network model of integrin $\alpha_V\beta_3$

The first step of the calculation is the formation of the elastic network model based on the x-ray crystal structure of integrin with a specific cutoff length. Motions of residues in this model depend on the number of neighboring residues. Residues with a small number of neighbors can move with less restraint compared to those with many neighbors. The number of the springs in molecules, which connect the C_α atoms in neighboring residues, depends on the cutoff length. Thus, the cutoff length is the most important parameter determining molecular motions.

As described in Materials and Methods, our definition of the distance between two residues is different from that in the conventional approach. Fig. 1 demonstrates the difference between the two approaches with a specific example. Two residue pairs in integrin, Gly^{172} and Ser^{225} in the α-chain, and Tyr^{274} in the α-chain and Leu^{258} in the β-chain, are shown in Fig. 1 *a* and *b*, respectively. The distances between the two C_α atoms (*black*) are 7.5 Å in both cases, whereas the shortest interatomic distances between the two residues in Fig. 1, *a* and *b*, are 7.0 and 3.3 Å, respectively. In the conventional approach, the two C_α atoms are connected by springs in both cases (assuming $R_c > 7.5$), whereas in our approach the C_α atoms in the former case are not connected and those in the latter case are connected (assuming $3.3 < r_c < 7.0$). Thus, the network formation is more sensitive to the local conformation in our approach.

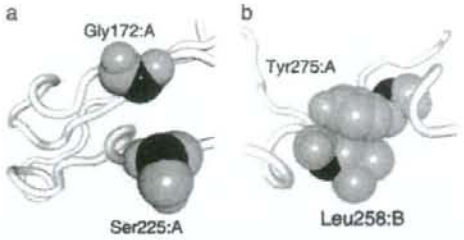

FIGURE 1 Two pairs of residues, Gly^{172} and Ser^{225} in the α-chain (*a*), and Tyr^{274} in the α-chain and Leu^{258} in the β-chain (*b*) in the x-ray crystal structure of integrin demonstrate the difference between the two approaches used to generate an elastic network model. The C_α atoms are colored in black, other atoms in gray. The backbone is represented by a white tube. In the conventional approach, the two residues in both cases are connected by a spring when the cutoff length, R_c, is >7.5 Å. In our approach, the residues in *b* are connected, whereas those in *a* are not, when the cutoff length, r_c, satisfies $3.3 < r_c < 7.0$.

A relatively large number of the pairs of residues are similar to the case shown in Fig. 1 *a*, that is, pairs of residues that have short C_α distances but long interatomic distances. For example, there are 774 pairs of residues in integrin in which the distances between the C_α atoms are between 7.5 and 8 Å, and these are usually regarded as neighboring residues according to the conventional approach. For 197 of these pairs of residues (25%), the shortest interatomic distances are >6 Å, and for 412 pairs (53%), the distances are >5 Å, which means that according to our approach, a fairly large number of the pairs of residues are not regarded as neighboring residues.

In this article, we studied the global conformational change of integrin from the bent to the extended conformation. Before we used our modified approach, we had used the conventional approach to build the elastic network model of the x-ray crystal structure of integrin with normal cutoff length ($R_c = 8$ Å) and had studied the molecular motions. However, we had not observed the motions that could direct the bent conformation of integrin to the extended one in the lowest-frequency normal modes. Some springs between residues must have hindered such motions. Thus, these springs should have been eliminated to promote the conformational change. We therefore tried to remove such springs from the elastic network model. However, it was not easy to find all such springs by eliminating springs one by one and checking the effect by NMA, because multiple springs could have been involved in the hindrance. Instead, we decreased the cutoff length so that springs representing interactions with longer distances would be eliminated, assuming that these interactions would be weaker and less important for the conformational change. To make this assumption more valid, we defined the distance between two residues as the shortest

interatomic distance, as described above. We will discuss the effect of the different definition later.

Dependence of molecular motions on cutoff length, r_c

NMAs were carried out for the elastic network models with various cutoff lengths, and the correlation coefficients were calculated based on Eq. 7. In Fig. 2, the calculated coefficients are plotted against the cutoff length as open circles connected by a solid line. The coefficients for cutoff lengths $>\sim$3.6 Å were roughly constant. However, at around r_c = 3.2–3.3 Å, the coefficients dropped abruptly. This cutoff length is roughly equivalent to the hydrogen bond distance, suggesting that the springs representing hydrogen bonds were on the verge of elimination in this range of cutoff lengths. A large correlation coefficient suggests that the molecular motions derived from the calculation are similar to those in the crystal structure, whereas a small coefficient suggests molecular motions that are different. We checked that the small coefficients did not stem from extremely large thermal atomic fluctuations, which are often observed for atoms with a small number of neighbors (data not shown).

The change of the molecular motions reflects the change of the energy landscape of the molecule, that is, the energy required for the conformational change from the x-ray crystal structure (bent structure) to the other conformations is altered. Thus, the conformational change to the extended one may become easier.

To identify the interactions that contributed to the sudden change of the coefficient, we eliminated the springs one by one by reducing the cutoff length starting from 3.3 Å, and NMA was performed. There were 231 springs that were to be eliminated when the cutoff length was reduced from 3.3 to 3.2 Å. We found the maximum drop in the coefficient when the spring connecting C_α atoms in Leu^{389} and Arg^{633} in the

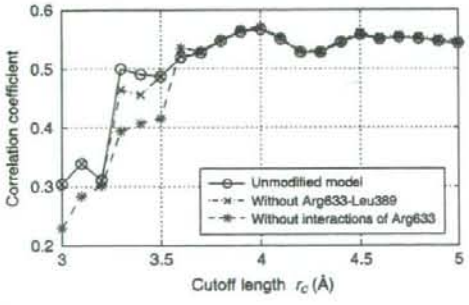

FIGURE 2 Correlation coefficient of the thermal atomic fluctuations derived from NMA and x-ray crystal structural data (B-factor) plotted against the cutoff length. Open circles connected by solid line: unmodified model. "X" symbols connected by dash-dotted line: model without interaction between Arg^{633} and Leu^{389}. Asterisks connected by dashed line: model without interactions between Arg^{633} and nearby nonbonded residues.

β-chain was eliminated, suggesting that the interaction represented by this spring has a large influence on the molecular motions.

The maximum drop in the coefficient observed when the interaction between Leu^{389} and Arg^{633} was eliminated does not mean that the drastic change in molecular motions would be caused by the elimination of the interaction at any cutoff length. If the longer cutoff length were assumed, other interactions would have had to be eliminated at the same time for the drastic change of the coefficient to occur. Thus, this result only suggests that the interaction between Leu^{389} and Arg^{633} was the one with the shortest distance that contributed to keeping the molecular motions as in the x-ray crystal structure. Indeed, the effect of eliminating the interaction between Leu^{389} and Arg^{633} independent of the cutoff length was limited, as shown in Fig. 2, where the correlation coefficients for the network models without the interaction between Leu^{389} and Arg^{633}, irrespective of the cutoff length, are plotted by "X" symbols connected by a dash-dotted line. We found that the effect was enhanced if the interactions of Arg^{633} with other nearby residues were simultaneously eliminated. In Fig. 2, the correlation coefficients are plotted by asterisks connected by a dashed line for the network models in which the C_α atom of Arg^{633} was not connected to the C_α atoms in the nearby nonbonded residues (including Leu^{389}) by springs. In the latter network models, the correlation coefficients were further deviated from those for the original models with full interactions (*open circles*) in the wider range of cutoff lengths. This suggests that the interactions of Arg^{633} with nearby residues have an influence on the molecular motions.

Change of lowest-frequency normal modes of integrin

The above analysis showed that the correlation coefficients dropped when the interactions of Arg^{633} were eliminated. However, it did not tell whether the drop was related to the biologically important conformational change of integrin, that is, the conformational change from the bent to the extended form. In this and the following subsections, we reveal what changed when the correlation coefficient dropped.

The change of the correlation coefficient is due to the change of the normal modes. To see what changed in the normal modes when the correlation coefficient dropped, we compared the lowest-frequency normal modes, which influence the global molecular motions, of the two elastic network models with different correlation coefficients.

The comparison was made for the two network models with and without the springs connecting the C_α atom of Arg^{633} to those in the nonbonded neighboring residues at the cutoff length of 3.4 Å (we call the former model A and the latter model B). At this cutoff length, the molecular motions of model A were similar to those in the x-ray crystal structure (Fig. 2, *open circles*), and by removing the springs of Arg^{633},

quite a large change in correlation coefficient was observed (*asterisks*), indicating that the springs were working as a switch for molecular motions.

A comparison of the five lowest-frequency normal modes for models A and B is shown in Table 1. It is clear that the second-, fourth-, and fifth-lowest-frequency normal modes of model B were similar to the first, second, and third modes of model A, respectively. The normal-mode frequencies were relatively close to each other. However, the first and the third modes of model B were not so similar to any of the five modes of model A. This result indicates that the new types of motions emerged once the interactions of Arg^{633} with other residues were eliminated.

The motion described by the lowest-frequency mode of model B is shown in Fig. 3 *a*. During this motion, the distance between the hybrid domain (Fig. 3, *deep green*; see also Figs. 4 and 8 *a*) and EGF-3 and EGF-4 (Fig. 3, *cyan*; see also Figs. 4 and 8 *a*) oscillated. Due to the springs from Arg^{633}, which connected the βTD (*cyan*; see also Figs. 4 and 8 *a*) with the hybrid domain near the head region (drawn beneath the hybrid domain in Fig. 3), the motions of the hybrid domain of model A were restrained, whereas those in model B were not. In this way, eliminating the interactions of Arg^{633} enhanced separation (opening motions) of the hybrid domain from the EGF domains. This opening motion might further induce elimination of the interactions between the hybrid domain and the EGF domains, which is shown to be important for the conformational change of integrin, as explained later.

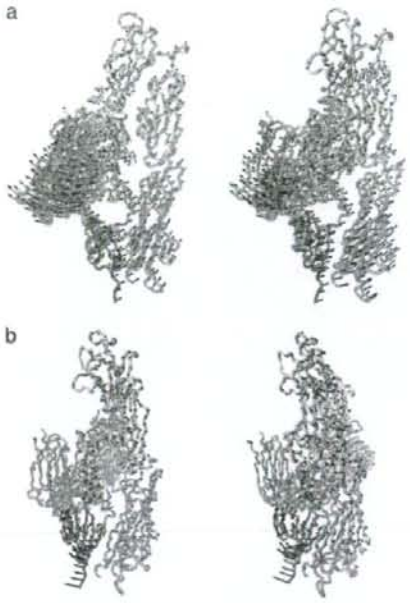

FIGURE 3 Displacement vectors of C_α atoms of integrin in the lowest- (*a*) and third-lowest- (*b*) frequency normal modes of model B (see text) drawn in stereo with the backbone. Leu^{375}, Leu^{389}, and Arg^{633} are shown by a space-filling model. The images were generated with a VMD program (62).

Role of inside-out signaling to local conformational change

Fig. 4 shows the local conformation around Arg^{633} (*cyan*) in the x-ray crystal structure. The residue Arg^{633} belongs to the βTD, and its side chain interacts with residues in the hybrid domain near the head region; the side chain of Arg^{633} is sandwiched by two leucine residues, Leu^{375} and Leu^{389} (*orange*), in the hybrid domain (see also Fig. 8 *b*). Our calculation suggests that the interactions of Arg^{633} with nearby residues influences the molecular motions. If the side chain of Arg^{633} is moved from the position in the x-ray crystal structure to a position where it is no longer sandwiched by the two residues, the interactions of Arg^{633} with nearby residues will be eliminated. Such a motion of the side chain of Arg^{633} was observed only in the third-lowest-frequency mode of the network model-B, as is shown in Fig. 3 *b*. This mode involved the motion of the βTD as a whole. Some external forces should be applied to move βTD and eliminate the interactions of Arg^{633}, to switch model A into model B.

TABLE 1 Comparison of the lowest-frequency normal modes of elastic network models A and B

		Model B				
	Frequency	0.72	0.73	1.36	1.66	2.01
Model A	1.00	0.25	**0.95**	0.02	0.01	0.14
	1.52	0.51	0.11	0.20	**0.82**	0.07
	1.99	0.41	0.00	0.32	0.26	**0.78**
	2.28	0.45	0.14	0.15	0.28	0.52
	2.58	0.32	0.10	0.56	0.35	0.04

Numbers >0.75 are shown in bold. The normal-mode frequencies are shown as relative values with respect to the lowest frequency of model A.

The x-ray crystal structure we used for NMA lacks the cytoplasmic domains and the transmembrane (TM) domains. Although the 3D structure of these domains is not so clear, there are abundant data indicating that the cytoplasmic domains can regulate integrin activation (45–53). These data show that integrin is activated if the membrane-proximal regions of the α and β cytoplasmic tails are separated, and that the interactions between these segments restrain the integrin in an inactive state. These studies were mainly performed on integrin $\alpha_{IIb}\beta_3$. The conformational rearrangement in the cytoplasmic domains should be transmitted to the ectodomains through the TM domains. However, little is known about the role of the TM domains in this process. Similar to the case of the cytoplasmic domains, modification of the membrane-proximal regions of ectodomain to inhibit the separation of the α- and β-chains restrains the activation, whereas enhancing the separation promotes activation (6,7,54).

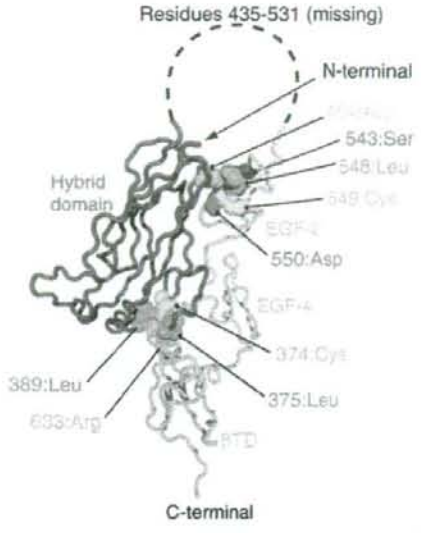

FIGURE 4 Three-dimensional structure of integrin β_3-chain. Arg^{633} and Arg^{404}, with their nearby residues, are shown by a space-filling model.

This experimental evidence is consistent with our results. Separation of the membrane-proximal regions of the α and β cytoplasmic tails, caused by binding of proteins such as talin (55–57), will cause rearrangement of the TM domains. This rearrangement will cause the conformational rearrangement of the βTD, which is close to the TM domain. If the rearrangement is similar to that shown in Fig. 3 *b*, the interactions of Arg^{633} with nearby residues will be eliminated, and the conformational change of ectodomain will be promoted. It is interesting to note that the motions shown in Fig. 3 *b* involve separation of the membrane-proximal regions of the α- and β-chains of the ectodomain, which has been shown to be important for integrin activation (6,7,54).

In Fig. 4, most of the residues involved in the interactions between the hybrid domain and the EGF domains are also indicated by the space-filling model. The amino acid residues that participate in the interactions are the same types as those in the interactions between the βTD and the hybrid domain, and in a similar way; a leucine (*orange*) and a cysteine (*yellow*) are adjacent to each other and in contact with the side chain of an arginine (*cyan*), which connects the two different domains. Compared to Arg^{633}, Arg^{404} is relatively exposed, and the area participating in the interactions is smaller.

Role of local interactions on the global conformational change

We deformed the x-ray crystal structure of integrin by iterative normal-mode calculations and studied the impact of eliminating the interactions we found above on the global conformational change from the bent to the extended forms. To clarify the set of interactions, we named the interactions between Arg^{633} and nearby residues "interaction A", and those between the hybrid domain and the EGF domains "interaction B". We performed four types of iterative normal-mode calculations, namely calculation with both A and B, calculation with A and without B, calculation without A and with B, and calculation without either A or B (Table 2). In all calculations, the cutoff length was set to 3.4 Å.

There are 25 disulfide bonds in the x-ray crystal structure of integrin. These bonds should not have broken during the iterative calculation. Thus, we kept the 25 springs between the residues that were covalently connected by the S-S bond.

In the x-ray crystal structure, residues between Asp^{434} and Lys^{532} in the β-chain were missing. During the iterative calculation, the distance between the two residues could become unrealistically long due to the lack of these residues. To prevent this happening, we added a spring between the C_α atoms in Asp^{434} and Lys^{532} whose spring constant was 1/10 that of the normal spring, assuming that the distance between the two residues was easier to change than those between nearby residues.

Two springs were eliminated in the four iterative calculations to enhance the conformational change. They were the spring between Val^{332} and Ser^{674} in the β-chain and that between Ser^{305} in the α-chain and Arg^{563} in the β-chain. These springs prevented the conformational changes when they were maintained in the calculations. The prevention of the conformational change by the former spring agrees with an experimental result, where the bent conformation was shown to be stabilized if the two residues (Val^{332} and Ser^{674}) were replaced by cysteines and a disulfide bond was formed (7). Even if the two residues were mutated so that they did not interact with each other, however, the ligand-binding affinity of integrin was not perturbed (T. Kamata, M. Handa, Y. Ikeda, and S. Aiso, unpublished data). Thus, the interactions did not play an active role in conformational change. Furthermore, even when the spring between Val^{332} and Ser^{674} was eliminated from the elastic network model for the x-ray crystal structure, new types of global motions, such as those observed when the springs of Arg^{633} were eliminated, did not emerge in the lowest-frequency range. These experimental and computational results suggest that the interactions be-

TABLE 2 Summary of four iterative normal-mode calculations

Calculation No.	Interaction A	Interaction B	Final conformation
1	–	–	Extended
2	–	+	L-shaped
3	+	–	Bent
4	+	+	Bent

Interaction A refers to the interactions of Arg^{633} with Cys^{374}, Gly^{388}, and Leu^{389}, and interaction B to those of Arg^{404} with Ser^{543}, Leu^{548}, Cys^{549}, and Asp^{550} plus the interactions between Glu^{364} and Ser^{551}. The plus and minus symbols mean that the springs representing these interactions exist or do not exist, respectively.

tween Val^{332} and Ser^{674} need to be eliminated for the conformational change of integrin, but that the elimination does not have the effect of enhancing the conformational change. The spring between Ser^{305} in the α-chain and Arg^{563} in the β-chain was eliminated for similar reasons. An experiment to replace a loop region in the α_{IIb}-chain, which corresponds to the loop including Ser^{305} in the α_V-chain, with that in the α_5-chain suggested that the interactions between Ser^{305} and Arg^{563} do not have an influence on the conformational change (58). Iterative normal-mode calculations showed that the spring needed to be eliminated for the conformational change. However, eliminating the spring from the elastic network model for the x-ray crystal structure had little effect on the lowest-frequency normal modes.

Among the four iterative calculations, integrin fully extended in one case, when the springs for both interactions A and B were eliminated (Fig. 5 *a*, and Table 2, *calculation 1*). In calculation 2 of Table 2, the conformational change terminated when the molecule took on an L-shape, as shown in Fig. 5 *b*. This result demonstrated the importance of eliminating interaction B for the conformational change to the fully extended form. The results of calculations 3 and 4 (Fig. 5, *c* and *d*) were quite similar. The corresponding structures (*n*th structures) during the iterative calculations were also similar to each other (rmsd < 3 Å). This result suggests that eliminating interaction B has a small effect on the conformational change if interaction A is maintained. The four iterative calculations clearly demonstrated that interaction A (interactions involving Arg^{633}) works as a snap to keep integrin in the bent form.

Comparison with the conventional elastic network model

Our elastic network model differs from the conventional model in the definition of the distance between two residues. We introduced this definition so that the network formation would be more sensitive to the local conformation, as described earlier. Here, to observe the effect of the difference in definition, we carried out the same calculations as those performed to obtain Fig. 2 using the conventional elastic network model. Decreasing the cutoff length tends to destabilize the elastic network model. To avoid this, we modified the conventional elastic network model by introducing springs, irrespective of the cutoff length, along the amino acid chain between C_α atoms in the *n*th and $(n + 2)$th residues and between those in *n*th and $(n + 3)$th residues, which is the same procedure as in our elastic network model. The calculated correlation coefficients are plotted against cutoff length R_c in Fig. 6. The coefficients were relatively large and roughly constant when the cutoff length, R_c, was >7.8 Å, indicating that the molecular motions derived from the calculations were similar to those in the crystal structure. In our elastic network model, the coefficient took similar values when the cutoff length, r_c, was >3.3 Å, as shown in Fig. 2. There were 8332 springs in the conventional model with $R_c =$ 7.8 Å, and 5512 springs in our elastic network model with $r_c = 3.3$ Å. The two network models had 5342 springs in common. Thus, the conventional model had 2990 additional springs and our model had 170 additional springs. The former springs correspond to the case shown in Fig. 1 *a*, but the latter do not correspond to any cases in Fig. 1. In the interactions represented by the latter case, amino acid residues with long side chains, such as Tyr or Arg, were often involved. The correlation coefficient between the thermal atomic fluctuations from the B-factors and those from the elastic network model, which was made from the common 5342 springs, was low (0.28). Thus, these additional springs were necessary in both models to reproduce the molecular motions in the crystal structure. However, there were obviously many more additional springs in the conventional model, suggesting that there were many springs in the conventional model that were not critically important for reproducing the molecular motions in the crystal structure.

Fig. 6 shows that the coefficient decreased noticeably as the cutoff length became shorter than 7.8 Å. However, the decrease was gradual compared to Fig. 2. In Fig. 2, the coefficient decreased by ~0.2 when the cutoff length was changed from 3.3 to 3.2 Å, whereas in this case, the same

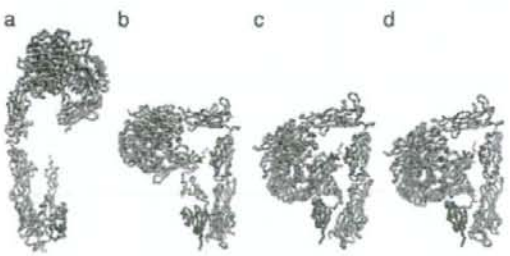

FIGURE 5 (*a–d*) Backbone structures of integrin at the end of iterative normal-mode calculations 1–4, respectively (Table 2).

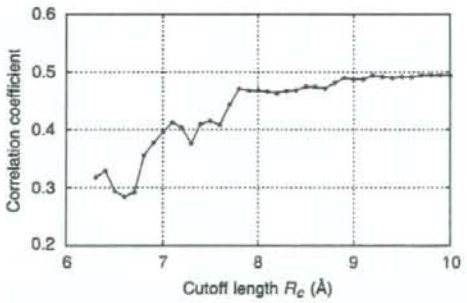

FIGURE 6 Correlation coefficient of the thermal atomic fluctuations derived from NMA and x-ray crystal structural data (B-factor) plotted against the cutoff length, R_c. Conventional elastic network models were used.

amount of decrease was observed only when the cutoff length was changed from 7.8 Å to 6.6 Å. Corresponding to the larger change in cutoff length to achieve the same amount of decrease of the coefficient, the number of the springs eliminated by the change in cutoff length was larger (1495 vs. 231). This result further supports the idea that there were more springs in the conventional elastic network model than in our model that did not critically influence the molecular motions.

The results presented here suggest that the short-distance interactions between two residues in our elastic network model have a potentially greater influence on the molecular motions than those in the conventional elastic network model, and thus that our definition of the distance between two residues is more effective than that in the conventional elastic network model in extracting or sorting such influential interactions, which is the major aim of this study.

Identifying key interactions for conformational change by NMA

Tama et al. (59) performed NMAs of the (conventional) elastic network models of proteins whose open and closed forms were solved by x-ray crystallography. They compared the atomic displacements in the conformational change from open to closed and closed to open forms with those in the normal modes. They found that the elastic network model for the open form generally had a normal mode in which the atomic displacements were close to those in the conformational change, whereas that for the closed form did not. In the case of integrin, there are two forms, that is, the bent form and the extended form. The former corresponds to the closed form, and the latter to the open form. The x-ray crystal structure was solved only for the bent form. Thus, if we consider the study by Tama et al. (59), what we did corresponds to the study to find the normal modes of the closed form of a protein that directed the molecule toward the open form. We found that the normal modes involved in the conformational change were newly generated by reducing the cutoff length until the correlation coefficients dropped drastically. Thus, our approach may be regarded as a possible solution for finding the normal modes of the closed form of a protein that direct the molecular structure toward the open form.

Instead of reducing the cutoff length, we can "manually" eliminate the interactions between domains of the elastic network model so that the extension of the molecule becomes easier. Assuming the cutoff length $r_c = 5$ Å, we performed NMA of the elastic network model. When all springs between the hybrid domain and the EGF/βTD domains were eliminated from this model, the correlation coefficient dropped from 0.54 (Fig. 2, *open circles*) to 0.34, and the lowest-frequency normal mode was similar to that shown in Fig. 3 *a* (with similarity of 0.75). This suggests that the "manual" elimination of interactions has an effect similar to the reduction of the cutoff length. However, without prior knowledge, it is difficult to decide which interactions should be eliminated.

Mutation experiments

Our calculations suggested that the interactions between Arg^{633} and the nonbonded nearby residues had to be eliminated for the structural rearrangement of integrin from the bent to the extended form to occur. Our calculations also suggested that the extension of integrin would be enhanced once the interactions were eliminated. To examine our predictions, specific interactions involving Arg^{633} were disrupted by mutating amino acid residues involved in the interactions.

Mutant $\alpha_{IIb}\beta_3$ was transiently expressed on the mammalian CHO cell surface and FITC-labeled fibrinogen-binding to these cells was examined. As shown in Fig. 7 *a*, wild-type $\alpha_{IIb}\beta_3$ expressed on the CHO cell surface was in a low-af-

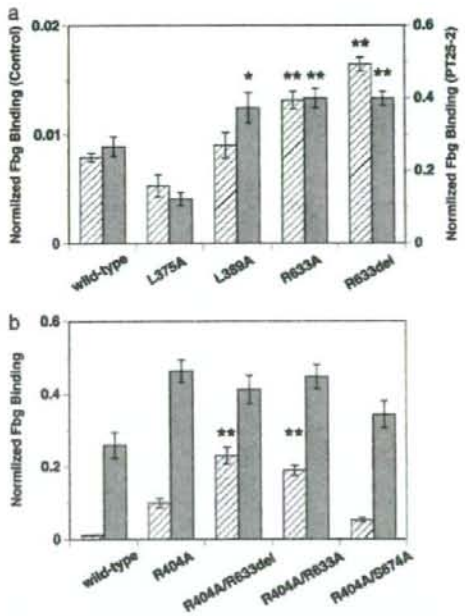

FIGURE 7 Average amount of FITC-labeled Fbg bound to CHO cells expressing wild-type or mutated $\alpha_{IIb}\beta_3$ obtained from six separate experiments. The amount of Fbg in the presence of control antibody (*hatched bars*) and PT25-2 (*shaded bars*) is shown separately in arbitrary units with error bars. (*a*) Results for mutations at the residues involved in the Arg^{633}-mediated interactions are compared with those for the wild-type. Amino acid residues Leu^{375}, Leu^{389}, and Arg^{633} in the β_3-chain were either mutated to Ala (*L375A*, *L389A*, and *R633A*) or deleted (*R633del*). The amount of Fbg in the presence of the control antibody and PT25-2 is shown in the left and right axes, respectively. Mutants that showed a statistically significant increase in binding from the wild-type are indicated by asterisks: $*p < 0.05$; $**p < 0.01$. (*b*) Results for single mutation of Arg^{404} in the β_3-chain (*R404A*) and double mutations of Arg^{404} in combination with either Arg^{633} (*R404A/R633A*, *R404A/R633del*) or Ser^{674} (*R404A/S674A*) are shown and compared with those for the wild-type. Mutants that showed significant increase in binding from the wild-type are indicated by asterisks: $**p < 0.01$.

finity state and did not bind to fibrinogen significantly unless activated by mAb PT25-2, which brought up the binding by ~33-fold. It has previously been shown that the mAb PT25-2 binds to the β-propeller domain of α_{IIb}-chain of integrin in platelets and induces the binding of integrin to fibrinogen (43,60). In contrast to the independent mutation of Leu^{375} or Leu^{389} to Ala, where the binding to fibrinogen was not affected so much, mutation of Arg^{633} to Ala, or its complete deletion, significantly increased the binding ($p < 0.01$). Activation with PT25-2 gave similar results, except that the L389A mutation showed a significant increase in binding ($p < 0.05$). These results indicate that the interactions involving the side chain of Arg^{633} are indeed important for constraining $\alpha_{IIb}\beta_3$ in a low-affinity state, as we predicted.

The mutations L375A and L389A did not activate $\alpha_{IIb}\beta_3$ (actually L375A with PT25-2 deactivated it, with $p < 0.01$). Because the degree of expression of integrin on the cell surface was not affected by these mutations, it is not probable that the mutations caused global conformational change. To find the reason for the low activation, we checked the thermal fluctuations of side-chain atoms in the arginine residues derived from the B-factor of the x-ray crystal structure. There are 62 arginines in the x-ray crystal structure. In most of the residues, the thermal fluctuations of the side-chain atoms farther away from the C_α atom are larger ($C_\beta < C_\gamma < C_\delta < \ldots$), suggesting the inherent flexibility of the side chain. Due to this flexibility, the side-chain atoms of Arg^{633} might be able to find new interaction sites in the mutated residue or in the nearby residues when Leu^{375} or Leu^{389} were mutated. In the case of L375A, the newly generated interactions might turn out to be stronger than the original and, as a result, $\alpha_{IIb}\beta_3$ might be further deactivated.

Our experimental results showed that complete elimination of the interactions involving Arg^{633} by deletion was not sufficient to fully activate $\alpha_{IIb}\beta_3$. According to our calculation, the elimination of Arg^{633}-mediated interactions alone would allow only halfway extension of integrin (Fig. 5 *b*); in other words, Arg^{633} is the key residue to initiate the extension, but not the key residue to complete the extension. Thus, the results from the mutational studies are consistent with our calculations. The calculation further showed that complete extension would be achieved if the interactions between the hybrid domain and EGF domains involving Arg^{404} were also eliminated (Fig. 5 *a*). To verify this calculation result, we introduced mutations on both Arg^{404} and Arg^{633} at the same time. Arg^{404} was mutated to Ala and Arg^{633} was either mutated to Ala or deleted. As a reference, we performed a double mutation on Arg^{404} and Ser^{674}, both of which were mutated to Ala, as well as a single mutation of Arg^{404} to Ala. The mutation of Ser^{674} is already known to have little effect on the activation, as discussed above. The results of the double mutations are almost exactly as we expected based on our calculations, as shown in Fig. 7 *b*. Compared to the single mutation R404A, the double mutations R404A/R633X (where X is A or del) clearly had larger effects ($p < 0.01$), which is in contrast to the effect of R404A/S674A, where the activity of integrin was not significantly different from the single mutations. The comparison between R404A/R633X and R404A/S674A demonstrates the importance of Arg^{633} again. These experimental and computational results suggest that the interactions at multiple interfaces have to be disrupted to achieve full activation as well as full extension.

It was demonstrated that $\alpha_V\beta_3$ and $\alpha_{IIb}\beta_3$ integrins are different in their signaling mechanisms (40). This difference may be partially explained by the different interactions between the cytoplasmic α and β tails, in addition to the difference between the molecules that may associate with the specific α cytoplasmic tails. Another report showed that extracellular calf-2/(EGF-4 and βTD) interface interactions affect manganese-induced activation differently in two β_3 integrins (61). These reports suggest that the α/β interface interactions have a significant impact on integrin activation and are responsible for the differential regulation in two β_3 integrins. Thus, the Arg^{633} mutations may not necessarily have the same effect on the $\alpha_V\beta_3$-ligand interaction as on the

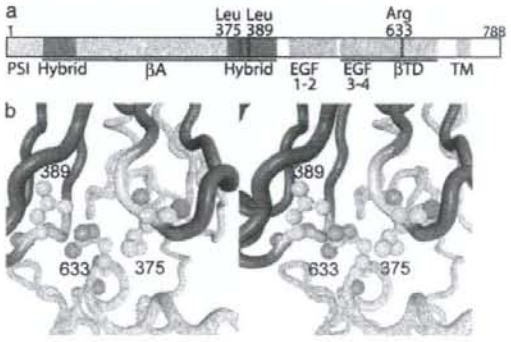

c

	375	389	633
β1	K	I	Q/E
β2	x	V	x
β3	L/Q	L	R/H/Q
β4	x	E/Q	E/D
β5	Q	L	x
β6	N/S	M	D
β7	x	V	x
β8	P	V	S/T

x : more than two types of aa
- : gap in the alignment

FIGURE 8 Conservation patterns of amino acid residues among different integrin β-chains at positions corresponding to positions 375, 389, and 633 of *H. sapiens* integrin β-chain. (*a*) A diagram of integrin β-chain to show domain organization and the location of residues 375, 389, and 633. Black bars below the diagram indicate regions observed with x-ray crystal structure. (*b*) Stereo figure of local structure around the three residues, showing that Arg^{633} is sandwiched by Leu^{375} and Leu^{389}. (*c*) Conservation pattern of residues in the three positions of mammalian integrin β-chain extracted from the multiple sequence alignment in Fig. 9. A slash in the column indicates that the position is occupied by one of the two or three amino acid residues, and x indicates that the position is not conserved in the group.

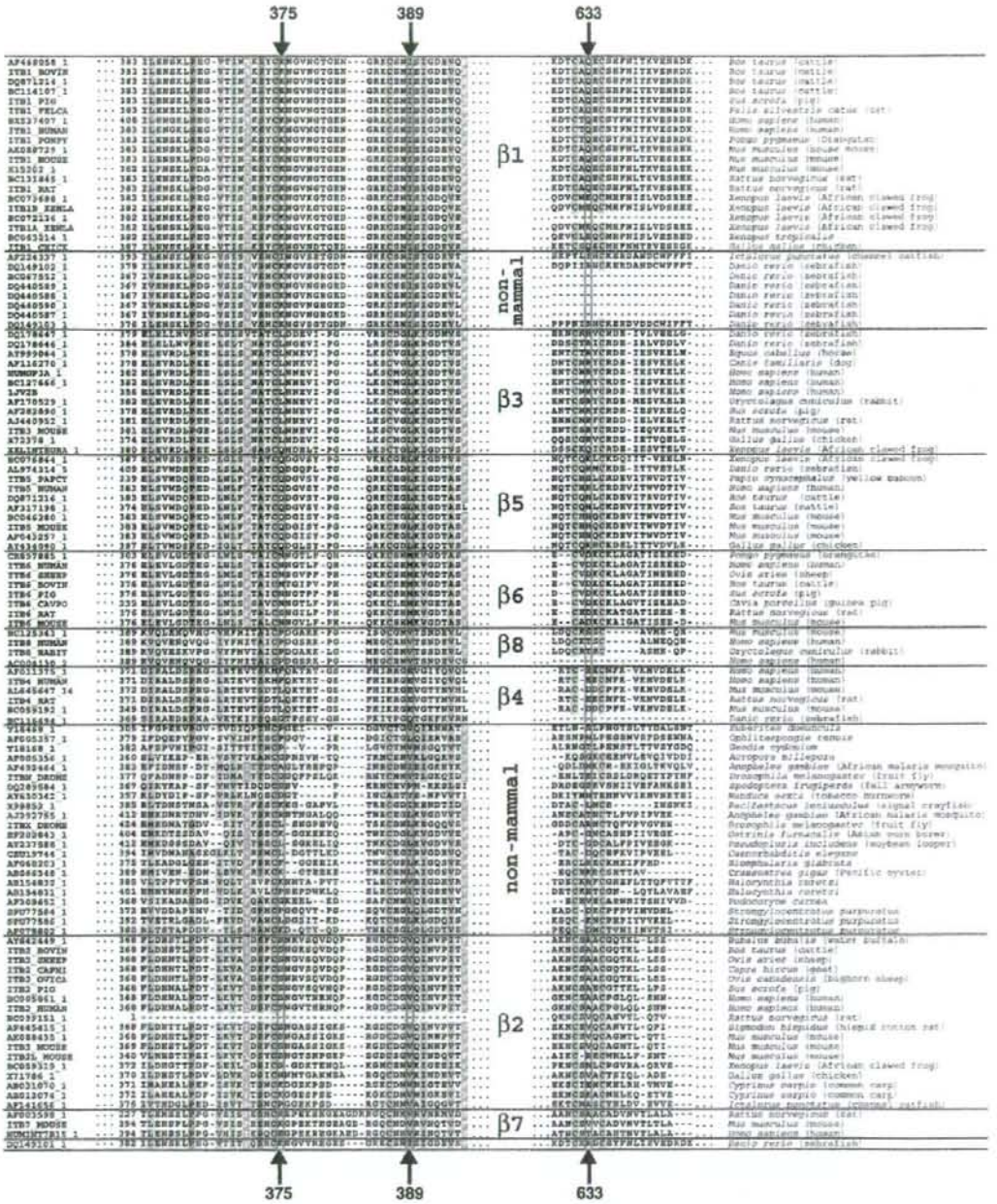

FIGURE 9 Multiple-sequence alignment of integrin β-chains. Regions around the residues concerned are shown. The key residues found in the β_3-chain by NMA on *H. sapiens* integrin $\alpha_V\beta_3$ and residues at homologous sites are boxed in red. Well conserved residues and cysteine residues in all the chains are highlighted. Identifications of each sequence in Genbank/UniProt/PDB are described on the left and the name of the species that the sequence is derived from is described on the right. The order of amino acid sequences is based on the sequence identity, and a horizontal bar separates groups in β-chains. The alignment around position 633 of β_4- and nonmammal chains was manually adjusted after automatic multiple-sequence alignment.

$\alpha_{IIb}\beta_3$-fibrinogen interaction observed in this study. However, the primary interdomain interactions that directly constrain $\alpha_V\beta_3$ integrin to the bent form in the crystal structure will be those of the hybrid domain with EGF and βTD domains, in which the interactions of Arg^{633} are included, and not those at the α/β interface. Thus, it is reasonable to assume that disrupting the Arg^{633}-mediated interactions has similar effects on the activation of $\alpha_V\beta_3$ as well.

Conservation patterns of residues in key interactions in the integrin β-chain

NMAs and mutation experiments on integrin suggested that the interactions of Arg^{633} in the β_3-chain with nearby nonbonded residues work as a snap to keep integrin in the bent form. Among the nearby residues, two leucine residues interact with Arg^{633} in an interesting manner, that is, they sandwich the side chain of Arg^{633} (Fig. 8 *b*). We checked the conservation pattern of these residues in homologous integrin β-chain sequences.

From the amino acid sequence databases, 113 sequences homologous to the *H. sapiens* integrin β_3-chain were retrieved and were clustered into 10 groups by a phylogenetic tree built on a multiple-sequence alignment (Fig. 9). Mammalian integrin β-chains are known to be classified into eight groups based on sequence similarity, ligand specificity, and expressed cells (1). Our results included two clusters of nonmammalian integrin β-chains, and eight other groups were consistent with the previous study. The set of key residues was conserved as Leu/Leu/Arg only in the integrin β_3-chain, and in other β-chains, the evolutionarily corresponding positions were either conserved with different amino acid residues or not conserved (Fig. 8 *c*).

Arginine has one of the longest aliphatic side chains in 20 amino acids, and hence, possible interactions between Leu and Arg are hydrophobic ones using aliphatic side chains (Fig. 8 *b*). The conservation patterns of other β-chains are dissimilar to those of the β_3-chain, which suggests that other β-chains may have different molecular mechanisms for the conformational transition or do not undergo a conformational change at all. β_1- and β_2-chains are known to undergo a similar type of bent-to-extended conformational transition, and we surmise that the molecular detail of the mechanism is different from that in β_3-chain.

CONCLUSION

The conformational change of integrin from the bent to the extended forms was studied by NMA of the elastic network model. The calculations revealed the key residues for the conformational change, and their importance was confirmed by the experiment. Multiple sequence alignment showed that the characteristic pattern of residues (Leu/Leu/Arg) was conserved only in the integrin β_3-chain, suggesting that the mechanism of the conformational change from the bent to the extended forms studied here is unique to the chain.

A pathway for the conformational change was speculated from the calculations, which is summarized as follows. The first step is the motion of the βTD as a whole (shown in Fig. 3 *b*), which is perhaps brought up by a signal from inside the cell (inside-out signaling). This motion involves the displacement of Arg^{633} in the β_3-chain, whose side chain is sandwiched by two leucine residues in the x-ray crystal structure. By this motion, the interactions of Arg^{633} with nearby nonbonded residues will be eliminated. Once the interactions of Arg^{633} are eliminated, the molecular motions change quite drastically. Specifically, the motions of the hybrid domain in the β_3-chain become dominant (Fig. 3 *a*). The motions will enhance the separation of the hybrid domain from the EGF domains and will contribute to the elimination of the interactions between these domains. If the interactions are eliminated, further drastic conformational change becomes easier, and the molecule will extend (Fig. 5 *a*).

We thank Ms. Sonomi Ito for her excellent technical assistance.

A.M., K.I., and K.Y. were supported by CREST, Japan Science and Technology Agency. T.K. was supported by a Health and Labor Science Research Grant for Research on Regulatory Science of Pharmaceuticals and Medical Devices from the Ministry of Health, Labor and Welfare, and by a Grant for Leading Project for Biosimulation from the Ministry of Education, Culture, Sports, Science and Technology of Japan.

REFERENCES

1. Hynes, R. O. 2002. Integrins: bidirectional, allosteric signaling machines. *Cell.* 110:673–687.
2. Ginsberg, M. H., D. Xiaoping, T. E. O'Toole, J. C. Loftus, and E. F. Plow. 1993. Platelet integrins. *Thromb. Haemost.* 70:87–93.
3. Xiong, J.-P., T. Stehle, B. Diefenbach, R. Zhang, R. Dunker, D. L. Scott, A. Joachimiak, S. L. Goodman, and M. A. Arnaout. 2001. Crystal structure of the extracellular segment of integrin $\alpha_V\beta_3$. *Science.* 294: 339–345.
4. Nermut, M. V., N. M. Green, P. Eason, S. S. Yamada, and K. M. Yamada. 1988. Electron microscopy and structural model of human fibronectin receptor. *EMBO J.* 7:4093–4099.
5. Du, X., M. Gu, J. W. Weisel, C. Nagaswami, J. S. Bennett, R. Bowditch, and M. H. Ginsberg. 1993. Long range propagation of conformational changes in integrin $\alpha_{IIb}\beta_3$. *J. Biol. Chem.* 268:23087–23092.
6. Takagi, J., H. P. Erickson, and T. A. Springer. 2001. C-terminal opening mimics "inside-out" activation of integrin $\alpha_5\beta_1$. *Nat. Struct. Biol.* 8: 412–416.
7. Takagi, J., B. M. Petre, T. Walz, and T. A. Springer. 2002. Global conformational rearrangements in integrin extracellular domains in outside-in and inside-out signaling. *Cell.* 110:599–611.
8. Brooks, B., and M. Karplus. 1983. Harmonic dynamics of proteins: normal modes and fluctuations in bovine pancreatic trypsin inhibitor. *Proc. Natl. Acad. Sci. USA.* 80:6571–6575.
9. Go, N., T. Noguti, and T. Nishikawa. 1983. Dynamics of a small globular protein in terms of low-frequency vibrational modes. *Proc. Natl. Acad. Sci. USA.* 80:3696–3700.
10. Levitt, M., C. Sander, and P. S. Stern. 1985. Protein normal-mode dynamics: trypsin inhibitor, crambin, ribonuclease and lysozyme. *J. Mol. Biol.* 181:423–447.

11. Tirion, M. M. 1996. Large amplitude elastic motions in proteins from a single-parameter, atomic analysis. *Phys. Rev. Lett.* 77:1905–1908.
12. Bahar, I., A. R. Atilgan, and B. Erman. 1997. Direct evaluation of thermal fluctuations in proteins using a single-parameter harmonic potential. *Fold. Des.* 2:173–181.
13. Tama, F., and C. L. Brooks III. 2002. The mechanism and pathway of pH induced swelling in cowpea chlorotic mottle virus. *J. Mol. Biol.* 318:733–747.
14. Tama, F., M. Valle, J. Frank, and C. L. Brooks III. 2003. Dynamic reorganization of the functionally active ribosome explored by normal mode analysis and cryo-electron microscopy. *Proc. Natl. Acad. Sci. USA.* 100:9319–9323.
15. Tama, F., and C. L. Brooks III. 2005. Diversity and identity of mechanical properties of icosahedral viral capsids studied with elastic network normal mode analysis. *J. Mol. Biol.* 345:299–314.
16. Wang, Y., A. J. Rader, I. Bahar, and R. L. Jernigan. 2004. Global ribosome motions revealed with elastic network model. *J. Struct. Biol.* 147:302–314.
17. Kim, M. K., R. L. Jernigan, and G. S. Chirikjian. 2003. An elastic network model of HK97 capsid maturation. *J. Struct. Biol.* 143:107–117.
18. Hinsen, K. 1998. Analysis of domain motions by approximate normal mode calculations. *Proteins.* 33:417–429.
19. Nishikawa, T., and N. Go. 1987. Normal mode of vibration in bovine pancreatic trypsin inhibitor and its mechanical property. *Proteins.* 2:308–329.
20. Durand, P., G. Trinquier, and Y.-H. Sanejouand. 1994. A new approach for determining low-frequency normal modes in macromolecules. *Biopolymers.* 34:759–771.
21. Lin, D., A. Matsumoto, and N. Go. 1997. Normal mode analysis of a double-stranded DNA dodecamer d(CGCGAATTCGCG). *J. Chem. Phys.* 107:3684–3690.
22. Matsumoto, A., M. Tomimoto, and N. Go. 1999. Dynamical structure of transfer RNA by normal mode analysis. *Eur. Biophys. J.* 28:369–379.
23. Matsumoto, A., and N. Go. 1999. Dynamic properties of double-stranded DNA by normal mode analysis. *J. Chem. Phys.* 110:11070–11075.
24. Matsumoto, A., and W. K. Olson. 2002. Sequence-dependent motions of DNA: a normal mode analysis at the base-pair level. *Biophys. J.* 83:22–41.
25. Matsumoto, A., I. Tobias, and W. Olson. 2005. Normal-mode analysis of circular DNA at the base-pair level. 1. Comparison of computed motions with the predicted behavior of an ideal elastic rod. *J. Chem. Theory Comput.* 1:117–129.
26. Matsumoto, A., I. Tobias, and W. Olson. 2005. Normal-mode analysis of circular DNA at the base-pair level. 2. Large-scale configurational transformation of a naturally curved molecule. *J. Chem. Theory Comput.* 1:130–142.
27. Matsumoto, A., and W. K. Olson. 2006. Predicted effects of local conformational coupling and external restraints on the torsional properties of single DNA molecules. *Multiscale Model. Simul.* 5:1227–1247.
28. Miyashita, O., J. N. Onuchic, and P. G. Wolynes. 2003. Nonlinear elasticity, proteinquakes, and the energy landscapes of functional transitions in proteins. *Proc. Natl. Acad. Sci. USA.* 100:12570–12575.
29. Tama, F., W. Wriggers, and C. L. Brooks III. 2002. Exploring global distortions of biological macromolecules and assemblies from low-resolution structural information and elastic network theory. *J. Mol. Biol.* 321:297–305.
30. Tama, F., O. Miyashita, and C. L. Brooks III. 2004. Flexible multi-scale fitting of atomic structures into low-resolution electron density maps with elastic network normal mode analysis. *J. Mol. Biol.* 337:985–999.
31. Hinsen, K., N. Reuter, J. Navaza, D. L. Stokes, and J. J. Lacapere. 2005. Normal mode-based fitting of atomic structure into electron density maps: application to sarcoplasmic reticulum Ca-ATPase. *Biophys. J.* 88:818–827.
32. McLachlan, A. D. 1979. Gene duplications in the structural evolution of chymotrypsin. *J. Mol. Biol.* 128:49–79.
33. The UniProt Consortium. 2007. The Universal Protein Resource (UniProt). *Nucleic Acids Res.* 35:D193–D197.
34. Sugawara, H., T. Abe, T. Gojobori, and Y. Tateno. 2007. DDBJ working on evaluation and classification of bacterial genes in INSDC. *Nucleic Acids Res.* 35:D13–D15.
35. Altschul, S. F., T. L. Madden, A. A. Schaffer, J. Zhang, Z. Zhang, W. Miller, and D. J. Lipman. 1997. Gapped BLAST and PSI-BLAST: a new generation of protein database search programs. *Nucleic Acids Res.* 25:3389–3402.
36. Barton, G. J., and M. J. Sternberg. 1987. A strategy for the rapid multiple alignment of protein sequences. Confidence levels from tertiary structure comparisons. *J. Mol. Biol.* 198:327–337.
37. Henikoff, S., and J. G. Henikoff. 1992. Amino acid substitution matrices from protein blocks. *Proc. Natl. Acad. Sci. USA.* 89:10915–10919.
38. Saitou, N., and M. Nei. 1987. The neighbor-joining method: a new method for reconstructing phylogenetic trees. *Mol. Biol. Evol.* 4:406–425.
39. Kimura, M. 1983. The Neutral Theory of Molecular Evolution. Cambridge University Press, London.
40. Ahrens, I. G., N. Moran, K. Aylward, G. Meade, M. Moser, D. Assefa, D. J. Fitzgerald, C. Bode, and K. Peter. 2006. Evidence for a differential functional regulation of the two β_3-integrins $\alpha_V\beta_3$ and $\alpha_{IIb}\beta_3$. *Exp. Cell Res.* 312:925–937.
41. Calvete, J. J. 2004. Structures of integrin domains and concerted conformational changes in the bidirectional signaling mechanism of $\alpha_{IIb}\beta_3$. *Exp. Biol. Med. (Maywood).* 229:732–744.
42. Ylanne, J., M. Hormia, M. Jarvinen, T. Vartio, and I. Virtanen. 1988. Platelet glycoprotein IIb/IIIa complex in cultured cells. Localization in focal adhesion sites in spreading HEL cells. *Blood.* 72:1478–1486.
43. Tokuhira, M., M. Handa, T. Kamata, A. Oda, M. Katayama, Y. Tomiyama, M. Murata, Y. Kawai, K. Watanabe, and Y. Ikeda. 1996. A novel regulatory epitope defined by a murine monoclonal antibody to the platelet GPIIb-IIIa complex ($\alpha_{IIb}\beta_3$ integrin). *Thromb. Haemost.* 76:1038–1046.
44. Kamata, T., A. Irie, M. Tokuhira, and Y. Takada. 1996. Critical residues of integrin αIIb subunit for binding of $\alpha_{IIb}\beta_3$ (glycoprotein IIb-IIIa) to fibrinogen and ligand-mimetic antibodies (PAC-1, OP-G2, and LJ-CP3). *J. Biol. Chem.* 271:18610–18615.
45. Crowe, D. T., H. Chiu, S. Fong, and I. L. Weissman. 1994. Regulation of the avidity of integrin $\alpha_4\beta_7$ by the β_7 cytoplasmic domain. *J. Biol. Chem.* 269:14411–14418.
46. Hughes, P. E., T. E. O'Toole, J. Ylanne, S. J. Shattil, and M. H. Ginsberg. 1995. The conserved membrane-proximal region of an integrin cytoplasmic domain specifies ligand binding affinity. *J. Biol. Chem.* 270:12411–12417.
47. Hughes, P. E., F. Diaz-Gonzalez, L. Leong, C. Wu, J. A. McDonald, S. J. Shattil, and M. H. Ginsberg. 1996. Breaking the integrin hinge. *J. Biol. Chem.* 271:6571–6574.
48. Kim, M., C. V. Carman, and T. A. Springer. 2003. Bidirectional transmembrane signaling by cytoplasmic domain separation in integrins. *Science.* 301:1720–1725.
49. Lu, C. F., and T. A. Springer. 1997. The α subunit cytoplasmic domain regulates the assembly and adhesiveness of integrin lymphocyte function-associated antigen-1. *J. Immunol.* 159:268–278.
50. Lu, C., J. Takagi, and T. A. Springer. 2001. Association of the membrane proximal regions of the α and β subunit cytoplasmic domains constrains an integrin in the inactive state. *J. Biol. Chem.* 276:14642–14648.
51. O'Toole, T. E., D. Mandelman, J. Forsyth, S. J. Shattil, E. F. Plow, and M. H. Ginsberg. 1991. Modulation of the affinity of integrin $\alpha_{IIb}\beta_3$ (GPIIb-IIIa) by the cytoplasmic domain of α_{IIb}. *Science.* 254:845–847.

52. O'Toole, T. E., Y. Katagiri, R. J. Faull, K. Peter, R. Tamura, V. Quaranta, J. C. Loftus, S. J. Shattil, and M. H. Ginsberg. 1994. Integrin cytoplasmic domains mediate inside-out signal transduction. *J. Cell Biol.* 124:1047–1059.

53. Ylanne, J., Y. Chen, T. E. O'Toole, J. C. Loftus, Y. Takada, and M. H. Ginsberg. 1993. Distinct functions of integrin α and β subunit cytoplasmic domains in cell spreading and formation of focal adhesions. *J. Cell Biol.* 122:223–233.

54. Xiong, Y.-M., J. Chen, and L. Zhang. 2003. Modulation of CD11b/CD18 adhesive activity by its extracellular, membrane-proximal regions. *J. Immunol.* 171:1042–1050.

55. Calderwood, D. A., R. Zent, R. Grant, D. J. G. Rees, R. O. Hynes, and M. H. Ginsberg. 1999. The talin head domain binds to integrin β subunit cytoplasmic tails and regulates integrin activation. *J. Biol. Chem.* 274:28071–28074.

56. Calderwood, D. A., B. Yan, J. M. de Pereda, B. G. Alvarez, Y. Fujioka, R. C. Liddington, and M. H. Ginsberg. 2002. The phosphotyrosine binding-like domain of talin activates integrins. *J. Biol. Chem.* 277: 21749–21758.

57. Vinogradova, O., A. Velyvis, A. Velyviene, B. Hu, T. A. Haas, E. F. Plow, and J. Qin. 2002. A structural mechanism of integrin $\alpha_{IIb}\beta_3$ "inside-out" activation as regulated by its cytoplasmic face. *Cell.* 110: 587–597.

58. Kamata, T., K. K. Tieu, A. Irie, T. A. Springer, and Y. Takada. 2001. Amino acid residues in the α_{IIb} subunit that are critical for ligand binding to integrin $\alpha_{IIb}\beta_3$ are clustered in the β-propeller model. *J. Biol. Chem.* 276:44275–44283.

59. Tama, F., and Y.-H. Sanejouand. 2001. Conformational change of proteins arising from normal mode calculations. *Protein Eng.* 14:1–6.

60. Puzon-McLaughlin, W., T. Kamata, and Y. Takada. 2000. Multiple discontinuous ligand-mimetic antibody binding sites define a ligand binding pocket in integrin $\alpha_{IIb}\beta_3$. *J. Biol. Chem.* 275:7795–7802.

61. Kamata, T., M. Handa, Y. Sato, Y. Ikeda, and S. Aiso. 2005. Membrane-proximal α/β stalk interactions differentially regulate integrin activation. *J. Biol. Chem.* 280:24775–24783.

62. Humphrey, W., A. Dalke, and K. Schulten. 1996. VMD: visual molecular dynamics. *J. Mol. Graph.* 14:33–38.

Cystathionine β-Synthase as a Carbon Monoxide–Sensitive Regulator of Bile Excretion

Tsunehiro Shintani,* Takuya Iwabuchi,* Tomoyoshi Soga, Yuichiro Kato, Takehiro Yamamoto, Naoharu Takano, Takako Hishiki, Yuki Ueno, Satsuki Ikeda, Tadayuki Sakuragawa, Kazuo Ishikawa, Nobuhito Goda, Yuko Kitagawa, Mayumi Kajimura, Kenji Matsumoto, and Makoto Suematsu

Carbon monoxide (CO) is a stress-inducible gas generated by heme oxygenase (HO) eliciting adaptive responses against toxicants; however, mechanisms for its reception remain unknown. Serendipitous observation in metabolome analysis in CO-overproducing livers suggested roles of cystathionine β-synthase (CBS) that rate-limits transsulfuration pathway and H_2S generation, for the gas-responsive receptor. Studies using recombinant CBS indicated that CO binds to the prosthetic heme, stabilizing 6-coordinated CO-Fe(II)-histidine complex to block the activity, whereas nitric oxide (NO) forms 5-coordinated structure without inhibiting it. The CO-overproducing livers down-regulated H_2S to stimulate HCO_3^--dependent choleresis: these responses were attenuated by blocking HO or by donating H_2S. Livers of heterozygous CBS knockout mice neither down-regulated H_2S nor exhibited the choleresis while overproducing CO. In the mouse model of estradiol-induced cholestasis, CO overproduction by inducing HO-1 significantly improved the bile output through stimulating HCO_3^- excretion; such a choleretic response did not occur in the knockout mice. ***Conclusion:*** **Results collected from metabolome analyses suggested that CBS serves as a CO-sensitive modulator of H_2S to support biliary excretion, shedding light on a putative role of the enzyme for stress-elicited adaptive response against bile-dependent detoxification processes.** (HEPATOLOGY **2009;49:141-150.**)

Carbon monoxide (CO) is generated from inducible heme oxygenase 1 (HO-1) and constitutive heme oxygenase 2 (HO-2), respectively, and has the ability to regulate neurovascular functions,[1,2] apoptotic responses,[3,4] and metabolism of xenobiotics and toxicants.[5,6] This gas is overproduced through increased delivery of heme as a substrate and the HO-1 induction on exposure to stressors such as hypoxia and oxidative stress. Mechanisms by which CO regulates cell functions appear to involve an activation of soluble guanylate cyclase (sGC), the enzyme that allows the gas to bind to the prosthetic heme to synthesize cyclic guanosine monophosphate as a second messenger.[1] Distinct from nitric oxide (NO) that forms 5-coordinated NO-Fe(II) complex to trigger full activation of the enzyme, CO activates this enzyme only modestly because the gas binding stabilizes 6-coordinated CO-Fe(II)-histidine complex.[7] Mitogen-activated protein kinase has also been shown to serve as a CO-responsive signal transducer.[8] Gene disruption of HO-1 increases sensitivity to overproduction of reactive oxygen species, inflammatory mediators or xenobiotic metabolism, whereas the gene transfer or CO inhalation under these circumstances suppresses such pathogenic responses.[7-9] However, direct mechanisms for the CO reception to trigger these adaptive responses of metabolism remain unknown.

Because this gas has the ability to inhibit ferrous form of the prosthetic heme of enzymes, tryptophan 2,3-dioxygenase or cytochromes P450 have been considered puta-

Abbreviations: CBS, cystathionine β-synthase; CE-MS, capillary electrophoresis equipped with mass spectrometry; CO, carbon monoxide; CORM, CO-releasing metal carbonyl tricarbonyldichlororuthenium (II); ES, 17α-ethinylestradiol; GSH, glutathione; GSNO, S-nitrosyl glutathione; H12, liver exposed to 12-hour hemin treatment; NO, nitric oxide; $RuCl_3$, CO-free ruthenium (III) chloride; SAM, S-adenosyl methionine; SE, standard error; sGC, soluble guanylate cyclase.

From the Department of Biochemistry and Integrative Medical Biology, Department of Surgery, School of Medicine, Keio University, Tokyo, Japan; the Institute for Advanced Biosciences, Keio University, Tsuruoka City, Japan; and the First Department of Surgery, College of Medicine, Nagoya University, Nagoya, Japan.

Received July 3, 2008; accepted August 25, 2008.

**These authors contributed equally to this work.*

T.H. is a postdoctoral research fellow supported by Grant-in-Aid for Creative Scientific Research 17GS0419 from JSPS in Japan. Development of the methodology for differential metabolomic analyses using contrast-enhanced time of flight/mass spectrometry was supported by Leading Project for Biosimulation from MEXT. T.I. and T.Y. are research associates of Global COE Program for Metabolomic Systems Biology from MEXT and MHLW.

Address reprint requests to: Makoto Suematsu, M.D., Ph.D., Professor and Chair, Department of Biochemistry and Integrative Medical Biology, School of Medicine, Keio University, 35 Shinanomachi, Shinjuku-ku, Tokyo 160-8582, Japan. E-mail: msuem@sc.itc.keio.ac.jp; fax: (81)-3-5363-3466.

Published online in Wiley InterScience (www.interscience.wiley.com).

DOI 10.1002/hep.22604

Potential conflict of interest: Nothing to report.